THESIS REPORT
Master's Degree

S Y S T E M S
R E S E A R C H
C E N T E R

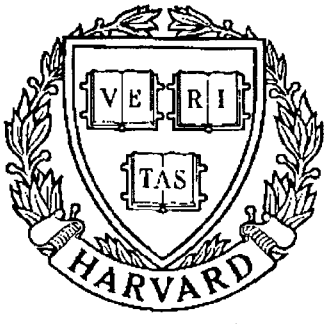

Supported by the National Science Foundation Engineering Research Center Program (NSFD CD 8803012), Industry and the University

Real-Time Control for a Zero Gravity Robotic End Effector

by: C. Salter
Advisor: J. Baras

M.S. 89-7
Formerly TR 89-108

Real-Time Control for a Zero Gravity Robotic End Effector

by

Carole Salter

Thesis submitted to the Faculty of The Graduate School
of The University Of Maryland in partial fulfillment
of the requirements for the degree of
Master of Science
1989

Advisory Committee:

Dr. John S.Baras Chairman/Advisor
Dr. William S. Levine
Dr. Mark A. Austin

ABSTRACT

Title of Thesis: Real-Time Control for a Zero Gravity Robotic End Effector

Name of Degree Canidate: Carole A. Salter

Degree and Year: Master of Science, 1989

Thesis directed by: Professor John S. Baras

Systems Research Center

Dept. of Electrical Engineering

There is no doubt that the task of gripping and handling objects in space is an important one. The ability to easily manipulate objects in a zero gravity environment will play a key role in future space activities. It is the aim of this research to develop control laws for the zero gravity robotic end effector designed by engineers at NASA Goddard. A hybrid force/position controller will be used. Sensory data available to the controller are obtained from an array of strain gauges and a linear potentiometer. Applying well known optimal control theoretic principles, the control which minimizes the transition time between positions is obtained. A robust force control scheme is developed which

allows the desired holding force to be achieved smoothly without oscillation. In addition, an algorithm is found to determine contact force and contact location.

DEDICATION

To my parents

ACKNOWLEDGMENTS

I would like to express my sincerest gratitude to those people who gave their assistance in the preparation of this thesis. In particular, to my advisor, Dr. John Baras, for both financial support and intuitive guidance. To John Vranish of the NASA Goddard Space Flight Center, whom the mechanical design of the gripper can be credited, for his constant encouragement and guidance. And to the rest of the NASA team including Richard Barclay, Michael Ali, Dipak Naik, and George Voellmer, whose help I sought frequently. Also to Yagyensh Pati and Dr. Anthony Lavigna for their insights into the theory and application of neural networks. And to the members of the thesis committee, Dr. William Levine and Dr. Mark Austin, for advice and direction on the force controller design.

I would like to acknowledge the support of the Systems Research Center and the Minta Martin Aerospace Research Fund through fellowships, and the Nasa Goddard Space Flight Center through a research grant.

On a more personal note, I would like to thank my parents for supporting

and encouraging me in my academic pursuits; my many friends, for putting up with me along the way; and especially, David MacEnany who has served as both mentor and good friend. Most of all, I would like to thank my fiancé Anthony Teolis for his unending patience and support. His generous help with various aspects of the preparation was invaluable.

TABLE OF CONTENTS

LIST OF TABLES

LIST OF FIGURES

CHAPTER
ONE

Introduction

There is no doubt that the task of gripping and handling objects in space [1] is an important one. Much diagnostic servicing and repair of existing space structures (e.g. satellites) require physical manipulation of the structure. Processing materials in space is an essential step in the evolution of space technology. With the goal of constructing large space structures in mind, earth based processing becomes both physically and economically impractical. This fact demands that the processing of materials be moved to the construction site ... into space.

Regrettably, direct human manipulation is also not a satisfactory solution. Though the various missions of the space shuttle have established the plausibility of humans working and living in space, the range of tasks achievable by direct human manipulation is limited. Moreover, machines are infinitely more suited to the many repetitive low-level tasks that may be required in space. Finally, the foreign environment of space presents a substantial health risk to a human manipulator.

[1] The term space will be used synonymously with the term "zero gravity environment".

It is evident, then, that robotic manipulation must play a vitally important role in the future of space activities. Already, telerobotic manipulators have been successfully employed in a full range of important space activities (e.g. satellite retrieval). Thus, the design of lightweight, dexterous robotic manipulators has become a significant and indispensable component of aerospace research and development in the past few years.

Designing the end effector portion of the *space manipulator*, one must address the problems associated with gripping objects in a zero gravity environment. The problems encountered here are very different and in many respects much more difficult than those encountered performing the same tasks on earth. Accordingly, the design and control of such end effectors must reflect these differences. Reaction forces and torques which are usually damped by various mechanisms (gravity, friction, interaction with the atmosphere) on earth, can create problems in space where these mechanisms are absent. For example, an astronaut attempting to turn a valve on a relatively large space vehicle must be securely attached to the vehicle, otherwise, instead of turning the valve, the torque created will serve to turn the astronaut relative to the vehicle. This is by no means the only difficulty. Consider the following scenario: A master slave arm is being used to link beams for a large space structure. The sockets used to link the beams are transported on trays to the locations of the beam joints. Due to the zero gravity environment, the sockets must be fixed in place by some

type of fastener to ensure they remain on the tray. Designing the end effector to release the fastener while maintaining a firm grasp on the socket will solve both the problems associated with torques and reaction forces, as well as the problem of minor perturbations dispersing the sockets in random directions.

Along this line of thinking, NASA has developed the *gripper/nut runner*. This specially designed end effector has two fingers which together have one degree of freedom. Similar to a vice, the width of the opening is the only variable. Centered between the fingers is a device for unscrewing nuts. Having one degree of freedom, the nut runner will be actuated by wrist rotations.

The aim of this research is to develop control laws (in some optimal sense) for the gripper/nut runner end effector. Control laws for the gripper and nut runner portions of the end effector may be developed independently since these two systems are decoupled. A hybrid force/position controller will be used for both the gripper and nut runner. Only the gripper controller is developed here. Sensory data available to the controller are obtained from an array of strain gauges as well as a linear potentiometer. Applying well known optimal control theoretic principles, the control which minimizes the transition time between positions is obtained. A robust force control scheme is developed for smoothly achieving the desired holding force without oscillation. An algorithm is found to determine contact force and contact location in order to ensure a secure grasp.

CHAPTER
TWO

End Effector Model

For analytical purposes it is necessary to establish a mathematical model of the system. The model development will be broken down into three sections. The first section details the actuator model. The basic model is standard and is available from various engineering texts. Added to the model in the second section are the effects of the gearing and the inertia of the mechanical system. Finally, the third section gives the complete system transfer function, as well as the position and force transfer functions.

2.1 Actuator Model

The finger actuator is a permanent-magnet DC motor. Models for these motors can be obtained from various sources [1], [2].

The armature is modeled by a resistance R_a, and inductance L_a, both in series with a voltage source ϵ_b representing the back emf generated by the rotor rotations. Applied to the armature terminals is the control voltage ϵ_a.

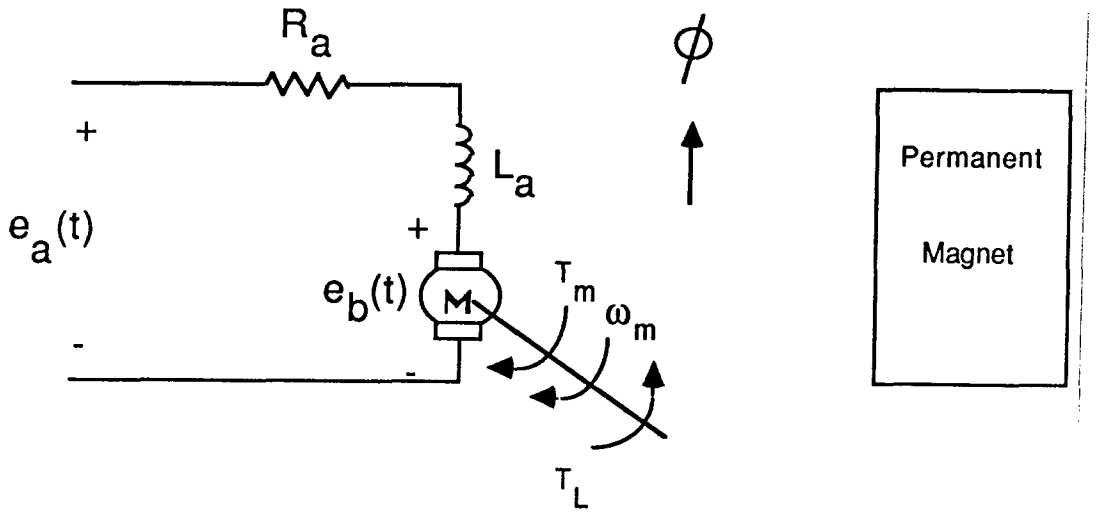

Figure 2.1: *Motor Model*

Proportional to the armature current by a constant k_i, the motor torque is given by

$$T_m(t) = k_i i_a(t). \tag{2.1.1}$$

Also, the back emf is proportional to the rotor angular velocity by constant k_b,

$$e_b(t) = k_b \omega_m(t). \tag{2.1.2}$$

In all DC permanent magnet motors there exists a ripple torque caused by the nonuniformity of the magnetic field. Thus the torque constant k_i is a function of the angular position of the rotor, and therefore periodic with period 2π. This periodic torque can effect the performance of the system; however, due to the high gear ratios being used, the effect is negligible.

constant	definition	value
R_a	armature resistance	25.2 Ω
L_a	armature inductance	7.2 mH
k_i	torque constant	0.0247 Nm/A
k_b	back emf constant	0.0247 $V/rad\ s^{-1}$
J_m	rotor inertia	$3.67 \times 10^{-7}\ kg\ m^2$
N	internal gear ratio	27.94
ϵ	internal gear efficiency	0.6

Table 2.1: *Motor Constants*

variable	definition
$e_a(t)$	control voltage
$i_a(t)$	armature current
$e_b(t)$	back emf
$\omega_m(t)$	angular velocity
$T_m(t)$	motor torque
$T_L(t)$	load torque

Table 2.2: *Motor Variables*

Applying D'Alembert's law at the motor output, and Kirchhoff's voltage law to the circuit model of the motor, the equations for the motor are as follows:

$$J_m\dot{\omega}_m(t) = T_m(t) - T_L(t) \tag{2.1.3}$$

$$L_a\dot{i}_a(t) = e_a(t) - R_a i_a(t) - e_b(t). \tag{2.1.4}$$

Selected for the actuation, the TRW 5A540-10 MM Planetary Gearmotor is manufactured with gears inside the motor housing (figure 2.2). The gearing has the effect of decreasing the angular velocity and increasing the torque. The gear ratio is 27.94 and the minimum efficiency is 0.6. A summary of the motor constants can be found in Table 2.1. Motor variables are summarized in Table

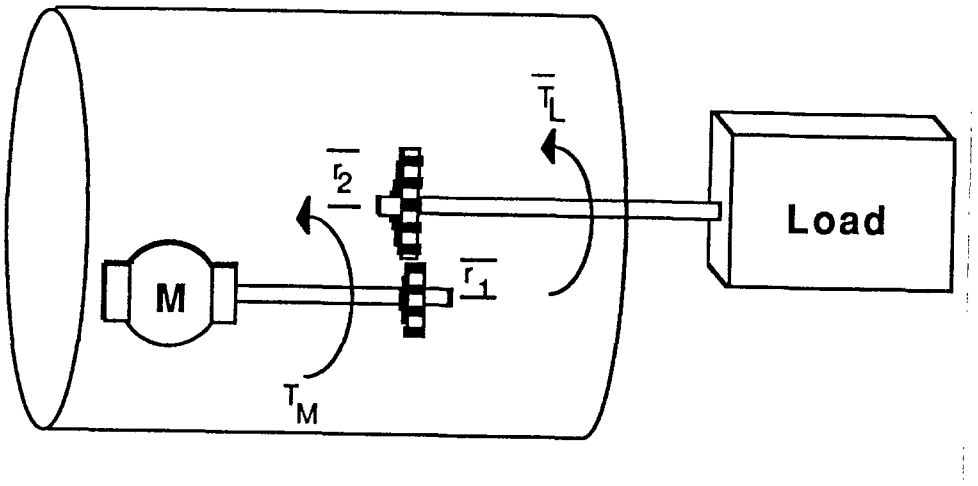

Figure 2.2: *Motor with Internal Gears*

2.2. Additional frictional terms have been neglected in the model development. They will be treated as disturbances to the control system.

A problem with the motor model developed above is that it gives the equations for the motor torque, $T_m(\cdot)$, and the motor angular velocity, $\omega_m(\cdot)$, disreguarding the effects of the internal gears. These equations must be modified to account for the gear effects. The modified equations will be in terms of $\bar{T}_m(\cdot)$ and $\omega_o(\cdot)$, the torque and angular velocity, respectively, of the motor output shaft accounting for the internal gearing.

Ideal gears are initially assumed in the derivation. A gear is termed ideal if it has no moment of inertia, no stored energy, no friction, and a perfect meshing of teeth.

Let $f_c(\cdot)$ denote the contact force where the gears mesh and $N = r_2/r_1$ the

constant	definition	value
$\bar{k}_i = \epsilon N k_i$	torque constant	$0.4141\ Nm/A$
$\bar{k}_b = N k_b$	back emf constant	$0.6901\ V/rad\ s^{-1}$
$\bar{J}_m = N^2 J_m$	rotor inertia	$2.9 \times 10^{-4}\ kg\ m^2$

Table 2.3: Equivalent Motor Constants

gear ratio (figure 2.2). From equation 2.1.3, with $T_L(t) = r_1 f_c(t)$, the equations for the motor and attached gear are

$$J_m \dot{\omega}_m(t) = T_m(t) - r_1 f_c(t) \tag{2.1.5}$$

$$\bar{T}_L(t) = r_2 f_c(t). \tag{2.1.6}$$

Combining these two equations, and using the geometric equality $\omega_m(t) = N\omega_o(t)$, gives

$$N^2 J_m \dot{\omega}_o(t) = N T_m(t) - \bar{T}_L(t). \tag{2.1.7}$$

Of course, in reality the gears are not ideal. To help account for this, an efficiency term, ϵ, is included in the equation as follows

$$N^2 J_m \dot{\omega}_o(t) = \epsilon N T_m(t) - \bar{T}_L(t). \tag{2.1.8}$$

By using the equivalent constants defined in Table 2.3 the adapted motor equations become

$$\bar{J}_m \dot{\omega}_o(t) = \bar{T}_m(t) - \bar{T}_L(t) \tag{2.1.9}$$

$$L_a \dot{i}_a(t) = e_a(t) - R_a i_a(t) - \bar{e}_b(t) \tag{2.1.10}$$

$$\bar{T}_m(t) = \bar{k}_i i_a(t) \tag{2.1.11}$$

$$\bar{e}_b(t) = \bar{k}_b \omega_o(t) \tag{2.1.12}$$

2.2 Mechanical Model

The transmission mechanism used is an acme screw. The acme screw serves to transform rotary motion of the motor to linear motion needed to move the fingers. A screw with a small lead angle, $\ell = 1.6\ mm$, was used so that larger finger tip forces could be developed while using a smaller motor. As a trade-off, the maximum velocity attained during opening and closing is lower. Another benefit of having a small lead angle is that the screw is self locking under reasonable load conditions. This is an important feature since it will allow the end effector to hold objects without using power. This property helps to eliminate problems created because of poor heat dissipation in space.

Used to link the motion of the fingers, the rack and pinion gear's effect is to move the fingers at the same velocity in opposite directions. The model, which is developed for the force and velocity of one of the fingers, is effected only by the efficiency, ρ, of this gear.

Deformations of the finger components are assumed to be negligible. This assumption is reasonable since operating forces are far below the magnitude necessary to result in significant deflections of the aluminum body. Because the motion is strictly linear the moving parts in the finger assembly are treated as a point mass located at the nut (figure 2.3). The mass of the moving parts is approximately $1.14\ kg$.

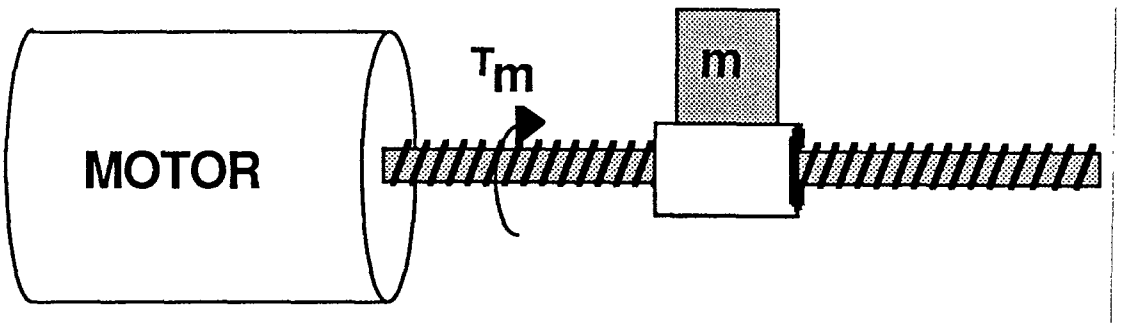

Figure 2.3: *System Diagram*

Since the errors due to backlash caused by the gears (the motor's internal gears, the acme screw, and the rack and pinion) will be within desired positioning accuracy of $\pm 0.25cm$, they can be ignored in the model development. Position control will be employed only to achieve an approximate desired finger opening; force control will be used upon encountering an object. Therefore, a coarse positioning scheme will be sufficient.

Completing the derivation of the system model, again assume initially ideal gears. For an ideal screw, the translation from angular velocity of the motor output shaft to linear velocity of the fingers is

$$V_L(t) = \frac{\ell}{2\pi}\omega_o(t) \tag{2.2.1}$$

and the transformation from torque to force is

$$F_c(t) = \frac{2\pi}{\ell}T_c(t) \tag{2.2.2}$$

where $T_c(\cdot)$and $F_c(\cdot)$ denote the coupling torque and force respectively between

the screw and the nut. Then developing the equations as before

$$\bar{J}_m\dot{\omega}_o(t) = \bar{T}_m(t) - T_c(t) \tag{2.2.3}$$

$$F_L(t) = F_c(t) - m\dot{V}_L(t) \tag{2.2.4}$$

Combining these equations and applying the screw equations 2.2.1 and 2.2.2 yields

$$F_L(t) = \frac{2\pi}{\ell}\bar{T}_m(t) - ((\frac{2\pi}{\ell})^2\bar{J}_m + m)\dot{V}_L(t) \tag{2.2.5}$$

As before efficiency terms, μ and ρ, are incorporated into the model to account for the losses in the non-ideal screw and rack and pinion gears respectively. For an acme screw the efficiency is approximately 0.4, and for the rack and pinion 0.7.

$$F_L(t) = \mu\rho\frac{2\pi}{\ell}\bar{T}_m(t) - ((\frac{2\pi}{\ell})^2\bar{J}_m + m)\dot{V}_L(t) \tag{2.2.6}$$

For simplification define

$$M \triangleq (\frac{2\pi}{\ell})^2\bar{J}_m + m \tag{2.2.7}$$

(2.2.8)

and

$$F_m(t) \triangleq \mu\rho\frac{2\pi}{\ell}\bar{T}_m(t) \tag{2.2.9}$$

yielding the final dynamic equation

$$F_L(t) = F_m(t) - M\dot{V}_L(t). \tag{2.2.10}$$

constant	definition	value
R_a	armature resistance	25.2 Ω
L_a	armature inductance	7.2 mH
$\bar{k}_i$	torque constant	0.4141 Nm/A
$\bar{k}_b$	back emf constant	0.6901 $V/rad\ s^{-1}$
M	effective mass	4473 kg
m	mass of moving parts	1.14 kg
N	internal gear ratio	27.94
ϵ	internal gear efficiency	0.6
ℓ	screw lead	1.6 mm
μ	screw efficiency	0.4
ρ	rack and pinion efficiency	0.7

Table 2.4: *Summary of System Constants*

By combining equations 2.1.10-2.1.12, 2.2.1 and 2.2.9 the final electrical equation is found to be

$$\mu\rho\bar{k}_i e_a(t) = \frac{\ell}{2\pi}(L_a\dot{F}_m(t) + R_a F_m(t)) + \mu\rho\bar{k}_i\bar{k}_b\frac{2\pi}{\ell}V_L(t) \tag{2.2.11}$$

A summary of the model constants is given in table 2.4.

2.3 System Transfer Functions

By taking the Laplace transform of equations 2.2.10 and 2.2.11 and rewriting them in matrix form, the system transfer matrix is:

$$\begin{pmatrix} F_m(s) \\ \\ V_L(s) \end{pmatrix} = \tag{2.3.1}$$

$$\frac{1}{\frac{\ell}{2\pi}(L_a s + R_a)Ms + \frac{2\pi}{\ell}\mu\rho\bar{k}_i\bar{k}_b} \begin{pmatrix} \frac{2\pi}{\ell}\mu\rho\bar{k}_i\bar{k}_b & \mu\rho\bar{k}_i Ms \\ \\ -\frac{\ell}{2\pi}(L_a s + R_a) & \mu\rho\bar{k}_i \end{pmatrix} \begin{pmatrix} F_L(s) \\ \\ e_a(s) \end{pmatrix}$$

Based on the model just derived, a hybrid force/position controller is developed in the following chapters. A hybrid controller operates under position

control unless a force is detected, in which case control is immediately given to the force controller. The force and position controllers can be developed separately and thus their individual transfer functions are given.

When calculating the position transfer function, $P(s) = sV_L(s)$, the output force, $F_L(s)$, can be assumed to be identically zero. This is justifiable since position control mode will only be used if there are no external load forces. The position transfer function is

$$\frac{P(s)}{e_a(s)} = \frac{\mu\rho\bar{k}_i}{s(\frac{\ell}{2\pi}ML_as^2 + \frac{\ell}{2\pi}MR_as + \frac{2\pi}{\ell}\mu\rho\bar{k}_i\bar{k}_b)}. \tag{2.3.2}$$

The force controller will only be used once a contact force has been detected on one of the fingers. Recall that the target object must be bolted firmly in place in a zero gravity environment. Thus once contact is made, position will become constant forcing the velocity to zero. From equation 2.2.10, this implies that the load force, F_L, equals the motor force, F_m. With these additional constraints the force transfer function is

$$\frac{F_m(s)}{e_a(s)} = \frac{\frac{2\pi}{\ell}\mu\rho\bar{k}_i}{L_as + R_a}. \tag{2.3.3}$$

CHAPTER

THREE

Position Controller

Available from a linear resistive potentiometer, the position information is accurate to $\pm.25$ *cm*. For the purpose of controller development further mechanical detail of this sensor is not needed.

3.1 Model Verification

By measuring the gripper's response to a series of sine waves of varying frequencies, the true Bode plot for position may be obtained. The true Bode plot is superimposed on the model Bode plot for position (figure 3.1). The accuracy of the true Bode plot for frequency greater than about 3 Hertz is extremely poor due to backlash in the system; this is essentially the *mechanical cutoff frequency* of the system. System performance will not be adversely affected by this low cutoff frequency since the fingers are not intended to make rapid changes in direction.

The actual Bode plot reveals that for the range of operation of the system, only first and possibly second order dynamics are evident. This implies that

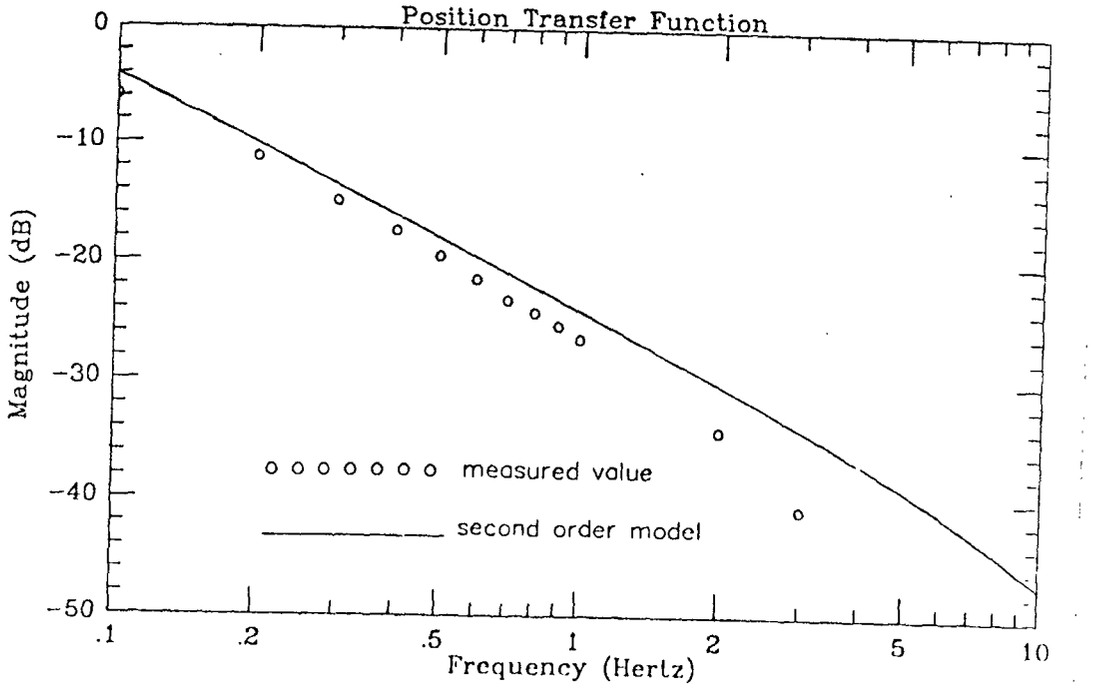

Figure 3.1: *Theoretical vs. Actual Position Transfer Function*

the third order dynamics caused by the nonzero inductance can be ignored, and thus it can be assumed that the inductance is zero when developing the position controller. Additional friction inherent in the system is apparent in the diminished response of the actual Bode plot.

3.2 State Space Realization

Substituting $L_a = 0$ into equation 2.3.2 gives:

$$\frac{P(s)}{e_a(s)} = \frac{\mu\rho\bar{k}_i}{s(\frac{\ell}{2\pi}MR_a s + \frac{2\pi}{\ell}\mu\rho\bar{k}_i\bar{k}_b)}. \tag{3.2.1}$$

Rewritten to simplify notation as

$$\frac{P(s)}{e_a(s)} = \frac{c_1}{s(s+c_2)}. \tag{3.2.2}$$

This transfer function describes a stable linear time invariant system which has one input, the control voltage $e_a(\cdot)$, and one output, the finger position $P(\cdot)$. The minimal realization has two states, finger position $P(\cdot)$, and finger velocity $V_L(\cdot)$. In state space form, the minimal system is written as

$$\begin{cases} \dot{\mathbf{x}}(t) = \mathbf{A}\mathbf{x}(t) + \mathbf{b}u(t) \\ y(t) = \mathbf{c}\mathbf{x}(t) \end{cases} \tag{3.2.3}$$

where

$$\mathbf{A} = \begin{pmatrix} 0 & 1 \\ 0 & -c_2 \end{pmatrix} \tag{3.2.4}$$

$$\mathbf{b} = \begin{pmatrix} 0 \\ c_1 \end{pmatrix} \tag{3.2.5}$$

$$\mathbf{c} = \begin{pmatrix} 1 & 0 \end{pmatrix}. \tag{3.2.6}$$

Note that since this realization is minimal, it is both controllable and observable. Also, stability of the system guarantees that the eigenvalues of $\mathbf{A}$ have nonpositive real part.

3.3 Optimal Position Controller

It is desirable to determine the control which moves the fingers from the initial state (position, velocity), $\mathbf{x}_0 = (\, x_0 \quad 0\,)'$, to the desired final state, $\mathbf{x}_f = (\, x_f \quad 0\,)'$, in minimum time. Such problems have been extensively studied in optimization theory. The solution to the minimum time problem follows from the well known Pontryagin Minimum Principle (PMP). The conditions on the time optimal control derived from the PMP for linear time invariant systems are detailed below [3].

3.3.1 Problem Statement

Given a completely controllable dynamical system

$$\dot{\mathbf{x}}(t) = \mathbf{A}\mathbf{x}(t) + \mathbf{b}u(t) \tag{3.3.1}$$

such that the control $u(t)$ is constrained in magnitude by the relation

$$|u(t)| \leq M \tag{3.3.2}$$

and that at the initial time $t_0 = 0$, the initial state of the system is $\mathbf{x}_0 \triangleq \mathbf{x}(t_0)$, find a control $u^*(\cdot)$ that transfers the system from $\mathbf{x}_0$ to $\mathbf{x}_f$ in minimum time. This control is called the time optimal control.

3.3.2 Optimality Conditions

Since the system is linear and controllable, a time optimal control, $u^*(t)$, that transfers the initial state $\mathbf{x}_0$ to $\mathbf{x}_f$ would clearly exist if there were no bounds on the control action. Even with the bounds on the control function, the reachable set at each finite time is convex and bounded and contains the origin. Therefore a time optimal control exists by simple translation of the origin. Existence of a time optimal control follows from the Bang-Bang theorem as well. Let $\mathbf{x}^*(t)$ denote the trajectory of the system corresponding to $u^*(t)$, originating at $\mathbf{x}_0$ at $t_0 = 0$, and hitting $\mathbf{x}_f$ in the minimum time, T^*. Then there exists a corresponding costate vector $\mathbf{p}^*(t)$ such that:

1. $\mathbf{x}^*(t)$ and $\mathbf{p}^*(t)$ are solutions of the canonical equations

$$\dot{\mathbf{x}}^*(t) = \frac{\partial H}{\partial \mathbf{p}^*}(\mathbf{x}^*(t), u^*(t), \mathbf{p}^*(t)) = \mathbf{A}\mathbf{x}^*(t) + \mathbf{b}u^*(t) \qquad (3.3.3)$$

$$\dot{\mathbf{p}}^*(t) = -\frac{\partial H}{\partial \mathbf{x}^*}(\mathbf{x}^*(t), u^*(t), \mathbf{p}^*(t)) = -\mathbf{A}'\mathbf{p}^*(t) \qquad (3.3.4)$$

with boundary conditions

$$\mathbf{x}^*(0) = \mathbf{x}_0, \qquad \mathbf{x}^*(T^*) = \mathbf{x}_f. \qquad (3.3.5)$$

The Hamiltonian function, H, is given by

$$H(\mathbf{x}(t), u(t), \mathbf{p}(t)) = 1 + < \mathbf{A}\mathbf{x}(t) + \mathbf{b}u(t), \mathbf{p}(t) > \qquad (3.3.6)$$

for linear time invariant systems.

2. The relation

$$H(\mathbf{x}^*(t), u^*(t), \mathbf{p}^*(t)) \leq H(\mathbf{x}^*(t), u(t), \mathbf{p}^*(t)) \tag{3.3.7}$$

holds for all admissible u(t) and for $t \in [0, T^*]$. From equation 3.3.6, this implies

$$\langle \mathbf{b}'\mathbf{p}^*(t), u^*(t) \rangle \ \leq \ \langle \mathbf{b}'\mathbf{p}^*(t), u(t) \rangle \tag{3.3.8}$$

holds for all admissible u(t) and for $t \in [0, T^*]$. Clearly, $< \mathbf{b}'\mathbf{p}^*(t), u(t) >$ is minimized by

$$u^*(t) = -Msgn(\mathbf{b}'\mathbf{p}^*(t)). \tag{3.3.9}$$

3. The relation

$$H(\mathbf{x}^*(t), u^*(t), \mathbf{p}^*(t)) = 0 \tag{3.3.10}$$

holds for all $t \in [0, T^*]$.

Thus it has been shown that the optimal control may only take on values $\pm M$, unless $\mathbf{b}'\mathbf{p}^*(t) = 0$ and then it is only constrained to be bounded in magnitude by M.

Since the system is linear and the constraints convex, the Pontryagin Minimum Principle provides both necessary and sufficient conditions for optimality. Finally the Hamiltonian has a unique global minimum (since it is a minimization of a linear function over a compact convex set). From this and the sufficiency it follows that the optimal control is unique.

3.3.3 Switching Time

The necessary conditions do not contain any explicit information regarding either the initial costate, $\mathbf{p}^*(0)$, or the terminal costate, $\mathbf{p}^*(T^*)$. However, from equations 3.3.6 and 3.3.10 it follows that the costate, $\mathbf{p}^*(t)$, must be a nonzero vector. That is

$$\mathbf{p}^*(t) \neq \mathbf{0} \quad \forall t \in [0, T^*]. \tag{3.3.11}$$

The set of feasible controls, $\mathcal{F}$, is practically limited by the maximum armature voltage, which implies $M = 24V$. And since $\mathbf{b}'\mathbf{p}^*(t) = c_1 p_2(t)$, and $c_1 > 0$, equation 3.3.9 implies that the set of feasible controls is

$$\mathcal{F} = \left\{ u : \begin{cases} u = M sgn(p_2(t)) & \text{if } p_2(t) \neq 0 \\ |u| \leq M & \text{if } p_2(t) = 0 \end{cases} \right\}. \tag{3.3.12}$$

Another physical constraint is that the control be continuous. Thus if p_2 changes sign the control must vary continuously from M to $-M$. The times at which $p_2 = 0$ are termed the *switching times*. The switching times vary with the initial and final states.

Solving equation 3.3.4 for the costate yields:

$$p_1^*(t) = p_1^*(0) = \text{constant} \tag{3.3.13}$$

$$p_2^*(t) = \left(p_2^*(0) - \frac{1}{c_2} p_1^*(0) \right) \exp(c_2) + \frac{1}{c_2} p_1^*(0) \tag{3.3.14}$$

Since $p_2^*(\cdot)$ is monotonic in t, the control voltage changes sign at most once. Without information of the initial or final costate, the switching time cannot be determined from these equations.

Disregarding the question of determining the initial or final costate, it is desirable to investigate which control among the feasible set, $\mathcal{F}$, steers the given initial state to the desired final state. Solving the state equation 3.3.4 yields

$$x_1(t) = x_0 + \frac{c_1 u(t)}{c_2} t + \frac{c_1 u(t)}{c_2^2}(1 - \exp(-c_2 t)) \tag{3.3.15}$$

$$x_2(t) = -\frac{c_1 u(t)}{c_2}(1 - \exp(-c_2 t)). \tag{3.3.16}$$

By substituting for $u(\cdot)$ in equations 3.3.15 and 3.3.16, one can determine the feasible control which achieves the desired goal. This control is the optimal control.

Notice that the optimal control is directly a function of time, and indirectly a function of position. In order to make the controller robust to disturbances, it is necessary that the dependence on position be made more precise. That is, a more desirable form for the control would be

$$u(x) = \begin{cases} 24 & x_0 \leq x \leq \alpha \\ -24 & \alpha < x \leq x_f \\ 0 & \text{elsewhere} \end{cases} \tag{3.3.17}$$

where α is the optimal *switching position* and x_0 and x_f are the initial and final positions respectively.

Using CONSOLE[1], a parametric optimization package, along with SIMNON, a nonlinear simulator, the optimal switching position α was determined. In every

[1]The implementation details of CONSOLE and SIMNON can be found in [4] and [5] respectively.

case the switching position was found to lie within the position error margins of $\pm.25\ cm$.

CHAPTER

FOUR

Force Controller

Strain gauges have been widely used in the field of stress analysis since 1940. They are one of the most accurate, sensitive, versatile and easy-to-use sensors available; but in spite of this, the proper and effective use of them requires a thorough understanding of their characteristics and performance [6].

Strain data is obtained from an array of four strain gauges on each finger (figure 4.1). From the strain data, both contact position and force can be calculated. This information will be used to control the holding force as well as to detect an improper grasp.

The ability to detect an improper grasp is important since a dropped object may not be easily retrieved. By calculating the contact force and contact locations the security of the grasp as well as the control action needed to correct any errors may be determined. Since the dimensions of the target objects are known, position information may be useful as well. Examples of possible grasp configurations are given in figure 4.2.

The following two sections present an introduction to strain gauges as force

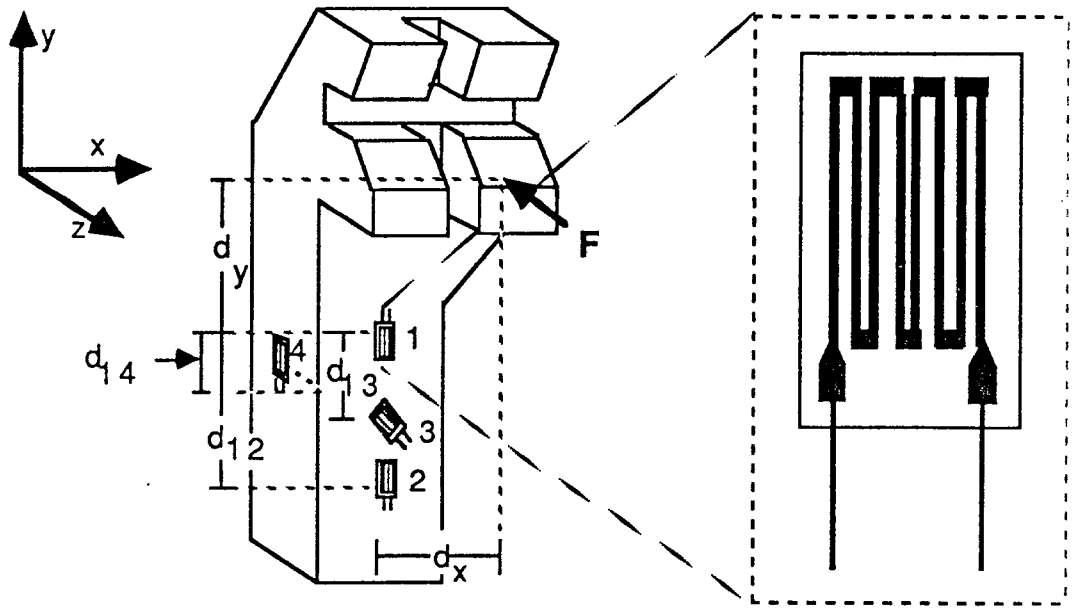

Figure 4.1: *Strain Gauge Positions*

sensors. Material is covered only in as much detail as necessary for the control design. A summary of some of the useful parameters and their values are found in table 4.1.

4.1 Surface Strains

Strain gauges are used to measure surface strains on a material. On any given surface three strain components may exist: normal strain ϵ_x in the x direction, normal strain ϵ_y in the y direction, and shear strain γ_{xy} (figure 4.3). The strain gauges used here measure unit normal strain[1] in the direction of the *sensitive*

[1] A strain/stress is termed normal to differentiate it from a shear strain/stress; it is common

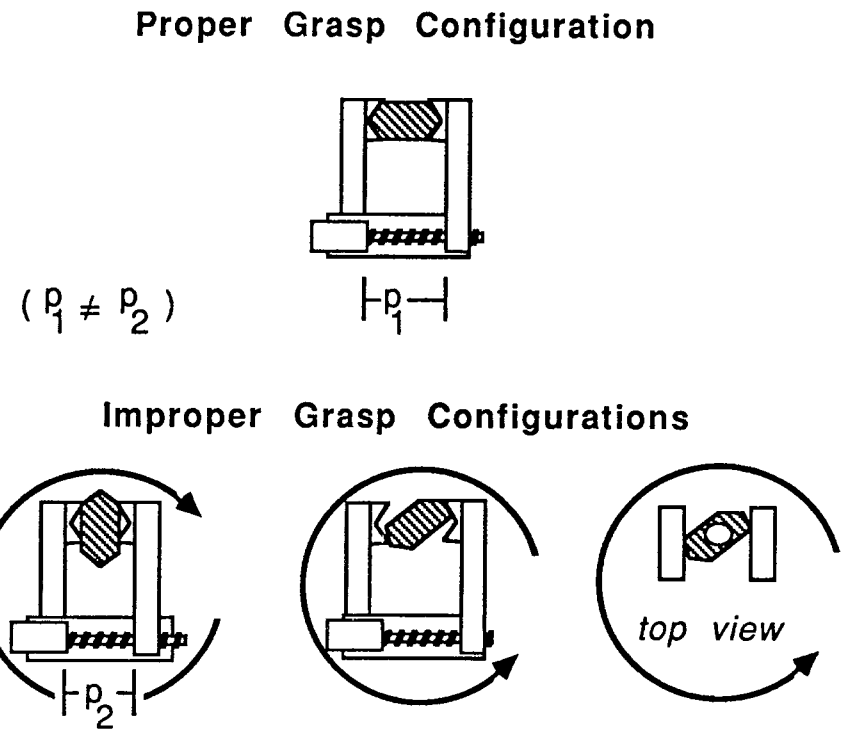

Figure 4.2: *Grasp Configurations*

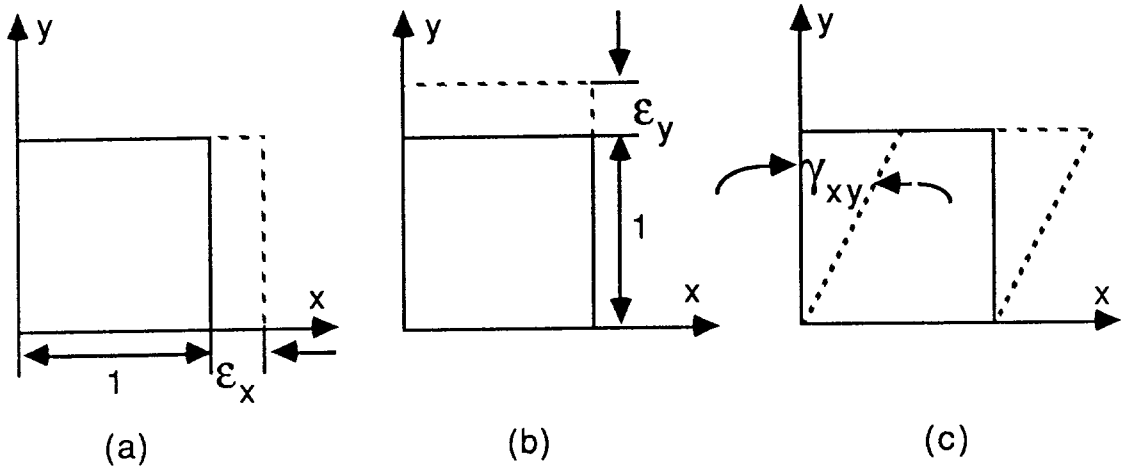

Figure 4.3: *Strains* ϵ_x, ϵ_y, *and* γ_{xy}.

constant/variable	definition	value
a	beam width	1.25 cm
b	beam depth	1.5 cm
d_{12}	distance between gauge 1 and 2	1.8 cm
d_{13}	distance between gauge 1 and 3	0.9 cm
d_{14}	distance between gauge 1 and 4	0.3 cm
E	Young's modulus for aluminum	10.4 N/m^2
ν	Poisson's ratio for aluminum	0.32
G	shear modulus for aluminum	3.93 N/m^2
d_z	horizontal distance: gauge 4 to force	2.5 cm
d_y^1	vertical distance: gauge 1 to force	
d_y^2	vertical distance: gauge 5 to force	
d_x^1	horizontal distance: gauge 3 to force	
d_x^2	horizontal distance: gauge 7 to force	
F	equivalent point contact force	
F_x	x component of F	
F_y	y component of F	
F_z	z component of F, $\perp$ to finger face	
M_x^1	$F_y d_z$ moment about x axis (finger 1)	
M_y^1	$F_x d_z + F_z d_x$ moment about y axis (finger 1)	
M_x^2	$-F_y d_z$ moment about x axis (finger 2)	
M_y^2	$F_x d_z + F_z d_x'$ moment about y axis (finger 2)	
γ_{xy}	shear strain in xy plane	
ϵ_x	strain in x direction	
ϵ_y	strain in y direction	

Table 4.1: *Force Sensor Parameters*

axis[2]. Unit strain is defined as the total deformation of the body in a given direction divided by the original length in that direction.

$$\epsilon = \frac{\Delta L}{L} \tag{4.1.1}$$

for the modifier normal to be omitted and this will be done henceforth in this paper.

[2]Though strain gauges are manufactured with most of the strain-sensitive filament aligned with the *sensitive axis* of the gauge, it is unavoidable that part of the grid is aligned transversely. This small transverse portion of the grid senses the strain at 90° to the sensitive axis and it's effects are superimposed onto the ideal data. The error is small, seldom exceeding 2 or 3% [7]. For the model derived here, this error is treated as a disturbance.

By applying Hooke's law to the strain measurements, it is possible to calculate the force. Hooke's law expresses the linear relationship between stress, force per unit area, and strain which is exhibited by many common materials under certain bounded loading conditions. Represented mathematically,

$$\sigma = E\epsilon \tag{4.1.2}$$

where E is a constant of proportionality known as the modulus of elasticity, or Young's modulus. A similar law, Hook's law in shear, relates shear stress and shear strain, again under bounded loading conditions.

$$\tau = G\gamma \tag{4.1.3}$$

The constant of proportionality G, termed the shear modulus of elasticity, is related to the modulus of elasticity, E, by

$$G = \frac{E}{2(1+\nu)}, \tag{4.1.4}$$

where ν is Poisson's ratio. Poisson's ratio is the constant ratio of strain in the lateral direction to strain in the longitudinal direction during tension or compression within the elastic range of a material.

4.2 Mechanical Model

In this section a functional mapping, $\widetilde{H}$, is derived to approximate the mapping

$$\epsilon = H\begin{pmatrix} \mathbf{F} \\ \mathbf{d} \end{pmatrix} : \mathbb{R}^6 \times \mathbb{R}^6 \mapsto \mathbb{R}^8 \tag{4.2.1}$$

where

$$\mathbf{F} = \begin{pmatrix} \mathbf{F}_1 \\ \\ \mathbf{F}_2 \end{pmatrix} : \quad \mathbf{F}_i \in \mathbb{R}^3, \qquad i = 1, 2$$

$$\mathbf{d} = \begin{pmatrix} \mathbf{d}_1 \\ \\ \mathbf{d}_2 \end{pmatrix} : \quad \mathbf{d}_i \in \mathbb{R}^3, \qquad i = 1, 2 \tag{4.2.2}$$

This mapping represents the continuous functional relation between the vector formed by the contact force and contact position on each finger, and the strains at the eight gauge locations. Taking into account the mechanical constraints of the physical situation, the dimensionality of this mapping can be reduced.

Assuming that the object has made contact with both fingers, the magnitude and direction of the x and z components of the contact force, with respect to each finger, will be the same. The y components will be equal in magnitude, but opposite in direction (figure 4.4).

$$\mathbf{F}_2 = \begin{pmatrix} F_{1x} \\ \\ -F_{1y} \\ \\ F_{1z} \end{pmatrix}. \tag{4.2.3}$$

(To simplify notation the subscript 1 will be deleted henceforth). The location of the contact on the face of each finger may be different but the z component is constrained by the mechanics of the gripper. Approximating the face of the gripper to be flat allows the z constraint to be taken as constant, i.e.

$$d_z = c \tag{4.2.4}$$

and

$$\bar{\mathbf{d}}_i = \begin{pmatrix} d_x^i \\ \\ d_y^i \end{pmatrix}, \quad i = 1, 2. \tag{4.2.5}$$

Thus knowledge of three force components and four position components is sufficient to approximate H. Hence the mapping $\widetilde{H}$ may be represented as

$$\epsilon = \widetilde{H} \begin{pmatrix} \bar{\mathbf{F}} \\ \\ \bar{\mathbf{d}} \end{pmatrix} : \mathbb{R}^3 \times \mathbb{R}^5 \mapsto \mathbb{R}^8 \tag{4.2.6}$$

with

$$\bar{\mathbf{F}} \in \mathbb{R}^3, \quad \bar{\mathbf{d}} = \begin{pmatrix} \bar{\mathbf{d}}_1 \\ \\ \bar{\mathbf{d}}_2 \\ \\ c \end{pmatrix} : \quad \bar{\mathbf{d}}_i \in \mathbb{R}^2 \quad i = 1, 2. \tag{4.2.7}$$

In order to determine the contact force and grip points given the strain gauge readings, the inverse mapping must be determined.

$$\begin{pmatrix} \bar{\mathbf{F}} \\ \\ \bar{\mathbf{d}} \end{pmatrix} = \widetilde{H}^{-1}(\epsilon) : \mathbb{R}^8 \mapsto \mathbb{R}^3 \times \mathbb{R}^5. \tag{4.2.8}$$

The detailed derivation follows.

By locating the strain gauges on the rectangular portion of the gripper finger, any effect induced by the irregular shape of the upper finger is nullified, and thus the finger can be modeled by a beam of rectangular cross section with width a, and depth b. Problems related to calculating the strains in rectangular beams have already been studied in depth in the fields of mechanical and materials engineering [8]-[9].

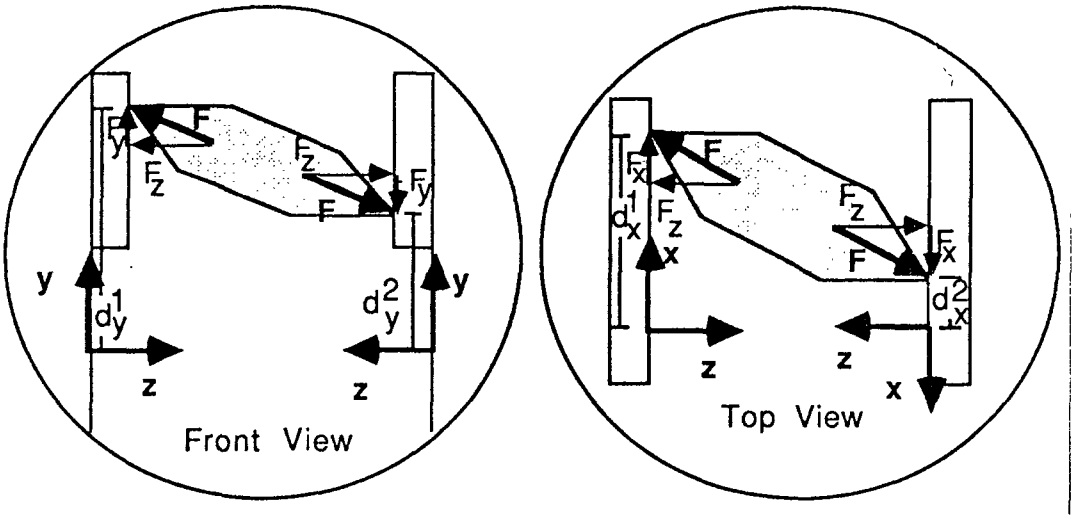

Figure 4.4: *Contact Force Vectors*

A contact force consisting of any combination of point contacts, line contacts, and surface contacts, may be represented by an equivalent single point contact with a specified contact force magnitude and location; thus it is sufficient to consider only single point contact forces. Each contact force, F, can be broken into three components, $[F_x\ F_y\ F_z]^T$. The z component is of greatest concern since this is the holding force. In a proper grasp both the x and y components should be zero.

To clarify the computations, the component forces and their induced moments will be treated separately (figure 4.5). The forces will be thought of as having equal magnitude and direction, but no horizontal offset from the vertical axis of the beam. In the y direction, the force causes tension or compression, while in the x and z directions, the forces induce bending. The corresponding

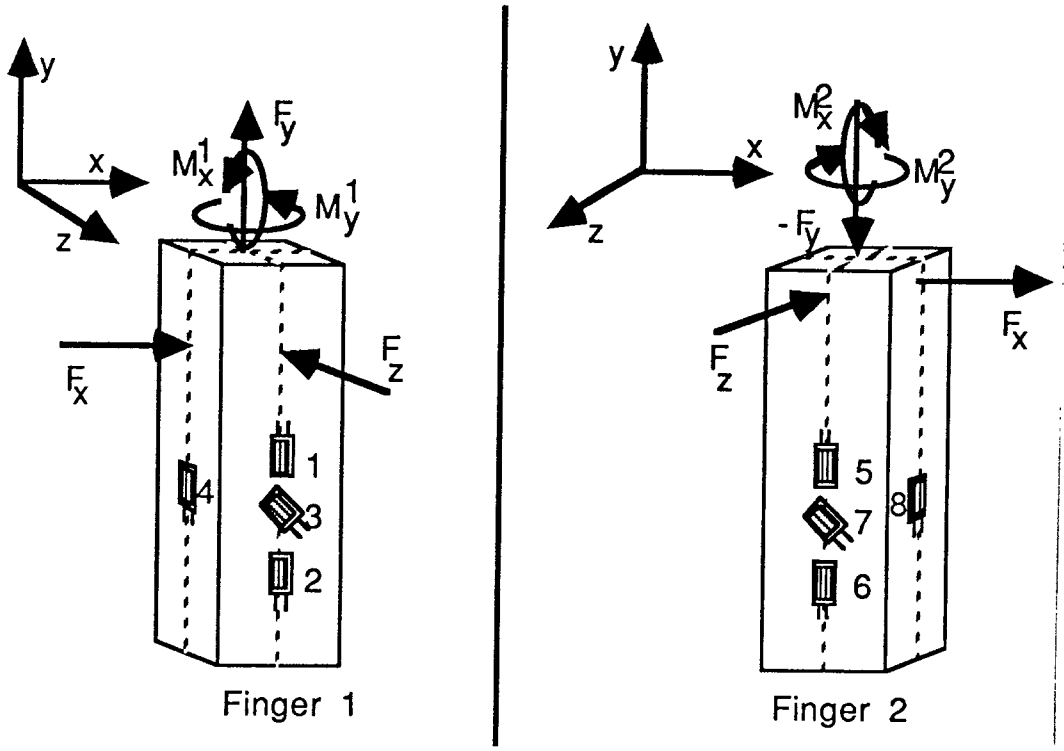

Figure 4.5: *Force and Moment Diagram*

moments, $M_x^1 = F_y d_z$, about the x axis, and $M_y^1 = F_z d_x + F_x d_z$, about the y axis, induce bending and torsion respectively (similarly for the moments M_x^2 and M_y^2 of finger 2). By applying superposition[3] the resultant effect of the tension/compression, the bending, and the torsion can be calculated by summing their separate effects.

To begin calculation of the forward mapping, $\widetilde{H}$, an explanation of the different types of strains caused by the contact force is given. The stress due to

[3]In general, the principle of superposition is valid for cases of loading where the magnitude of the stress and deflection is directly proportional to the load.

bending in a rectangular beam is given by σ

$$\sigma = \frac{M}{S}, \tag{4.2.9}$$

where M is the bending moment and S is the section modulus. For a rectangular beam the section modulus is

$$S = \frac{ba^2}{6}. \tag{4.2.10}$$

Combining these equations with Hooke's law, equation 4.1.2, an equation for the strain due to bending moment M is determined to be:

$$\epsilon = \frac{6M}{ba^2E}. \tag{4.2.11}$$

In cases of nonuniform bending a shear strain is induced in the 'sides' of the beam. Nonuniform bending occurs if the moment is not constant throughout the beam. This is the case when the moment is generated by a force, F, on the beam; the moment varies with distance from the force. For a rectangular beam this has been determined (see [9]) to be

$$\gamma_{xy} = \frac{3F}{2abG}. \tag{4.2.12}$$

The stress due to a tensile/compressive force, P, in a rectangular beam is

$$\sigma = \frac{P}{ba}. \tag{4.2.13}$$

Again applying Hooke's law, the strain is

$$\epsilon = \frac{P}{Eba}. \tag{4.2.14}$$

The torsion created by the y axis moment, M, will cause only shear strain in the xy coordinate reference frame. An approximation for the shear strain (on the front center of each finger) is given as in [9] by

$$\gamma_{xy} = \frac{M}{0.235ba^2G}. \tag{4.2.15}$$

Oriented vertically on the finger, gauges 1, 2, 4, 5, 6, and 8 are not affected by torsion (figure 4.1). Gauges 3 and 7 though, are affected by the torsion as well as the the other strains. Oriented at 45° to the coordinate axis, these gauges are aligned with the principle axis of pure torsion; thus the strain measured due to torsion is maximized.

Applying equations 4.2.11 and 4.2.14, equations for the strains[4] at gauge location i, $i \in \{1, 2, 5, 6\}$ are as follows:

$$\epsilon_1 = \frac{6F_z d_y^1}{ba^2E} + \frac{F_y}{baE} + \frac{6F_y d_z}{ba^2E} \tag{4.2.16}$$

$$\epsilon_2 = \frac{6F_z (d_y^1 + d_{12})}{ba^2E} + \frac{F_y}{baE} + \frac{6F_y d_z}{ba^2E} \tag{4.2.17}$$

$$\epsilon_5 = \frac{6F_z d_y^2}{ba^2E} - \frac{F_y}{baE} - \frac{6F_y d_z}{ba^2E} \tag{4.2.18}$$

$$\epsilon_6 = \frac{6F_z (d_y^2 + d_{12})}{ba^2E} - \frac{F_y}{baE} - \frac{6F_y d_z}{ba^2E}. \tag{4.2.19}$$

The first term in each equation is due to the nonuniform bending induced by the force F_z. The second is due the tension/compression induced by the force F_y. And the third is due to the uniform bending moment about the x axis associated with F_y.

[4]The sign convention adopted here assigns tensile strains a positive value. Care must be taken when developing the strain equations since a positive force may cause compression at the location on the finger where the measurement is taken.

The equations for the strains at gauge location i, $i \in \{4, 8\}$, on the side of the gripper finger, follow similarly from equations 4.2.11 and 4.2.14:

$$\epsilon_4 = \frac{6F_x(d_y^1 + d_{14})}{ba^2E} + \frac{F_y}{baE} \tag{4.2.20}$$

$$\epsilon_8 = \frac{-6F_x(d_y^2 + d_{14})}{ba^2E} - \frac{F_y}{baE}. \tag{4.2.21}$$

Again, the first term is due to the nonuniform bending which, in this case, is induced by the force F_x. And, just as above, the second term is due to the tensile strain induced by the force F_y.

The calculations for gauges 3 and 7 are a little more complicated. The strains that are described thus far have been determined with respect to the xy coordinate reference frame. In order to derive a formula for the strain measured at strain gauges 3 and 7, the contribution of strains in the xy reference frame to the normal strain in a frame rotated $-45°$ must be determined. This derivation can be found in reference [9]. With θ the angle of relative orientation of the coordinate frames,

$$\epsilon_\theta = \epsilon_x \cos^2(\theta) + \epsilon_y \sin^2(\theta) + \gamma_{xy} \sin(\theta)\cos(\theta). \tag{4.2.22}$$

Letting $\theta = -45°$, and applying the equation at gauge locations 3 and 7

$$\epsilon_3 = \frac{1}{2}\left(\frac{6F_z(d_y^1 + d_{13})}{ba^2E} + \frac{F_y}{baE} + \frac{6F_y d_z}{ba^2E} - \frac{3F_x}{2abG} - \frac{F_z d_x^1 + F_x d_z}{0.235ba^2G}\right) \tag{4.2.23}$$

$$\epsilon_7 = \frac{1}{2}\left(\frac{6F_z(d_y^2 + d_{13})}{ba^2E} - \frac{F_y}{baE} - \frac{6F_y d_z}{ba^2E} - \frac{3F_x}{2abG} - \frac{F_z d_x^2 + F_x d_z}{0.235ba^2G}\right) \tag{4.2.24}$$

To help clarify this derivation, equation 4.2.23 has been broken down into

its components.

$$\epsilon_x = 0 \tag{4.2.25}$$

$$\epsilon_y = \frac{6F_z(d_y^1 + d_{13})}{ba^2E} + \frac{F_y}{baE} + \frac{6F_y d_z}{ba^2E} \tag{4.2.26}$$

$$\gamma_{xy} = \frac{3F_x}{2abG} + \frac{F_z d_x^1 + F_x d_z}{0.235ba^2G} \tag{4.2.27}$$

The equation for ϵ_y is derived exactly the same way as equations 1.2.16-4.2.19. The first shear strain term is caused by the nonuniform bending induced by the force F_x. The second term is due to the torsion caused by the moment M_y. The derivation is identical for ϵ_7.

Now given the strain measurement from gauges 1 and 2, or gauges 5 and 6, the magnitude of the holding force, F_z, can be calculated,

$$F_z = \frac{ba^2E(\epsilon_2 - \epsilon_1)}{6d_{12}} = \frac{ba^2E(\epsilon_6 - \epsilon_5)}{6d_{12}}. \tag{4.2.28}$$

The calculation of the inverse mapping for the other components was accomplished using the symbolic algebra package MACSYMA. Due to the length and complexity of these equations, they will not be given here. Knowledge of their existence is sufficient for the purposes of this paper.

4.3 Determination of Holding Force and Contact Location

In the previous section it was proven theoretically that knowledge of the output of the eight strain gauges is sufficient to uniquely determine the location

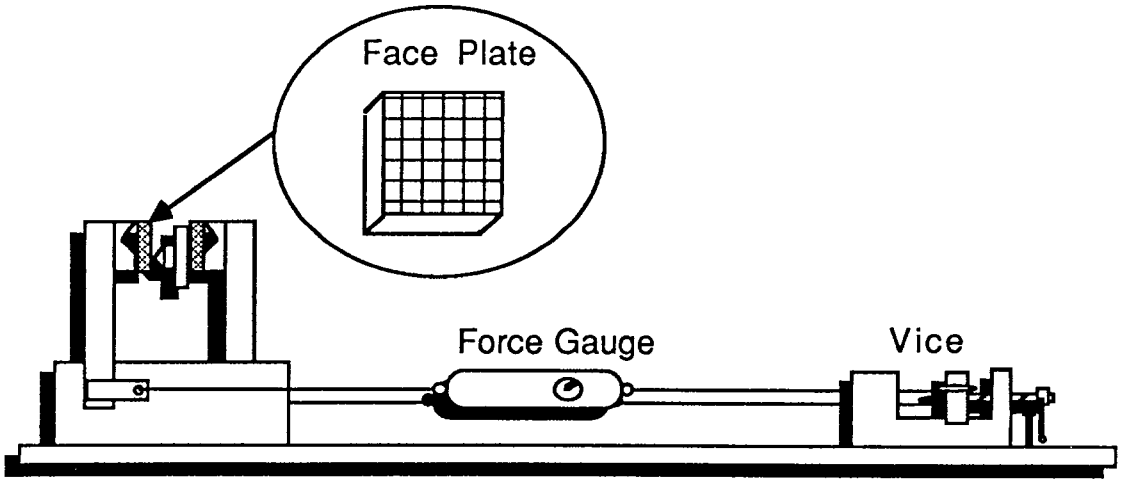

Figure 4.6: *Experimental Setup for Accurate Force Measurements*

and magnitude of the contact force on both fingers. Unfortunately, the accuracy of the derived model may be affected by various disturbances caused by the unmodeled effects of transverse sensitivity, gauge misalignment, zero drift, and temperature dependence, the accuracy of the derived model may be effected. A controller design based on experimentally measured data should be more robust to these disturbances.

An experimental setup for accurately applying forces, F_z, perpendicular to the face of the gripper finger is depicted in figure 4.6. With this setup it is possible to empirically measure the sensor output for various holding force magnitudes and positions. Then, from the data, the functional relationship

$$\begin{pmatrix} \bar{\mathbf{F}} \\ \bar{\mathbf{d}} \end{pmatrix} = \widetilde{H}^{-1}(\epsilon) : \mathbb{R}^8 \mapsto \mathbb{R}^3 \times \mathbb{R}^5 \tag{4.3.1}$$

can be determined. Note that for this setup F_x and F_y are both zero.

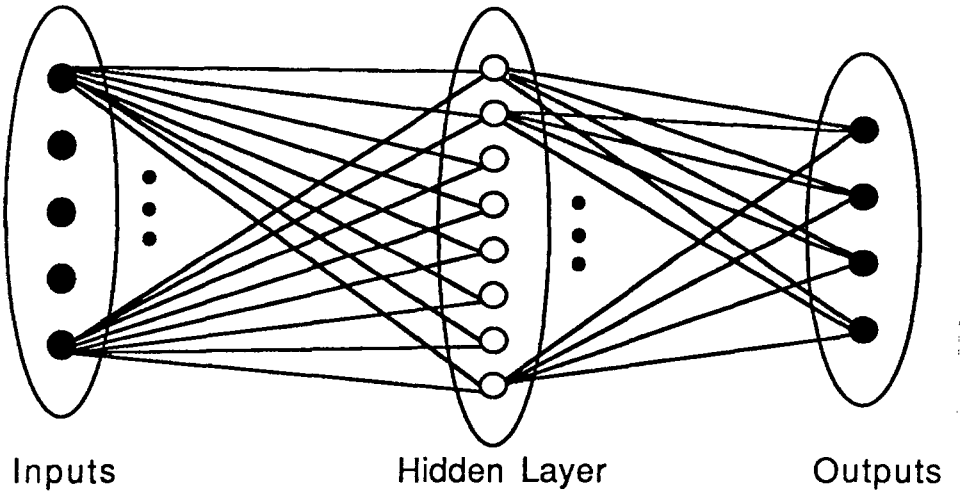

Figure 4.7: *Feed Forward Neural Net*

The equations developed in section 4.2 which express this relation mathematically are nonlinear (and continuous). The approximation of a continuous nonlinear function is a natural application for neural networks [5]. It has been shown by Cybenko [11], that continuous functions of finite support may be approximated by a feed forward neural network with a single (finite) hidden layer (figure 4.7). It is thus justified that this topology be used here. Whereas the functional approximation problem could be solved by choosing the form of the solution to be like the model and adjusting the parameters; the neural net solution has the additional advantage that the form of the solution need not be assumed.

[5] An in depth discussion of neural networks is beyond the scope of this paper. An excellent introductory reference is the book by Rumelhart and McClelland [10]. A brief introduction is given in Appendix A. The information is covered in only as much detail as necessary for a clear understanding of the particular neural network used in this application.

The sufficiency proof in Cybenko's paper is nonconstructive and thus does not indicate the required number of neurons in the hidden layer. Using gradient descent (back propagation) to set the weights, the number of neurons is set by trial and error (i.e. If the network can converge to the solution given by the data in the training set, there are enough neurons in the hidden layer.).

For the case with F_x and F_y both zero, the network solution is found (see chapter 5).

4.4 Force Controller

Only knowledge of the holding force, F_z, is necessary for force control. Once the desired holding force has been attained at both fingers the contact locations and other force components can be calculated. There are several reasons for this control scheme. First, knowledge of the holding force is sufficient for the task of securing the grasp; knowledge of the contact locations and other force components is necessary only for assuring a proper grasp. Second, the holding force can be calculated as linear combination of the readings from gauges 1 and 2, or gauges 5 and 6 (equation 4.2.28). The calculation complexity for the other variables is much higher, and involves readings from more of the strain gauges. Both the additional readings and calculations are time expensive and their incorporation into the control loop should be avoided if possible. Third, the contact locations and other force components cannot be determined unless

contact is made to both fingers. In the case where contact is made to only one of the fingers, the gripper must be moved to center the object between the fingers *before* the contact location and other force components can be calculated.

Because the surfaces of the gripper fingers are not compliant, attempting to implement a minimum time controller may cause oscillation. Instead an attempt will be made to achieve a smooth response.

The model of the force response, as derived in Chapter 2, is that of an asymptotically stable first order system. Such a system is robust to parameter variation, since the only effect of parameter variation would be to translate the poles of the force transfer function in the open left half plane.

A typical controller for a first order system is a simple high gain controller. Theoretically, any finite positive gain could be chosen without destabilizing the system, however, chosing a gain which is *too large* may cause instability due to unmodeled dynamics. In addition, the gain is physically limited by the constraint on maximum armature voltage of $24V$.

The force sensors are the most significant possible cause of feedback destabilization of the force control loop. This is due to the slow response exhibited by the strain gauges when a large force is applied then taken away. Once the force has been removed, the strain gauges may still detect its presence for a very short time. This could easily lead to oscillation. To avoid this a *dead band* can

be put in the control algorithm such that if the measured force is *close enough* to the desired force, no control action will be taken.

CHAPTER
FIVE

Hardware Implementation

Developing hardware for space applications is a demanding task. In addition to those problems caused by a zero gravity environment, there are a host of others due to the harsh ambient variations associated with earth orbit. A satellite in geosynchronous orbit about the earth is subjected to variations in temperature alone in excess of several hundred degrees centigrade. Specifically, temperature specifications for the space station hardware state that all equipment must be able to withstand temperatures of $-150°C$ for 28 minutes and temperatures of $200°C$ for 55 minutes during each 83 minute orbit of the earth.

In such an environment, standard mechanical methods used for earth based devices are inappropriate. For instance, the viscosity of typical mechanical lubricants varies wildly with temperature rendering them useless in space.

Reliability becomes another significant concern in space engineering. From a purely monetary standpoint, an operation failure in a relatively inexpensive component can potentially disable the entire mechanism. Apart from fault-tolerant engineering considerations (e.g. redundant design), it is imperative

that each component be of the highest quality.

Named above are only a few of the peculiarities associated with working in space. Although these considerations are crucial to a practical working device, the initial design phase may relax some of the specifications. Based more on financial than technical reasons, components which do not quite meet specifications were chosen for the prototype. For example, a brushed DC motor was substituted for a brushless DC motor. These substitutions should not adversely effect the control methods and algorithms developed here.

5.1 Position Sensor

Position information is measured using a linear potentiometer. A potentiometer is a sliding contact resistive transducer which converts the mechanical displacement into an electrical output. This is accomplished by changing the effective length of the resistive element by moving a brush which maintains electrical contact as it moves.

The resistive element is formed by wrapping a resistive wire around a nonconductive element; the turns must be spaced to prevent shorting. As the brush slides across from one turn to the next, the output voltage increases in steps, as does the resistance. This determines the available resolution. With a minimum theoretical resolution of .025 cm, the errors in position due to the potentiometer will fall within the accepted position uncertainty of $\pm.25$ cm.

The term *linear* refers to the linearity of the output voltage as a function of position. This implies that the resistance measured between one of the ends of the element and the brush contact is a direct linear function of the contact position in relation to that end. In practice, the relation is only approximately linear but the deviations are within the error margins of this application.

Using an analog to digital (A/D) converter this information is made available to the control algorithm. The equation which relates the sensor reading to gripper opening in centimeters was calculated by direct measurements to be:

$$\text{opening} = 6.9 \times 10^{-3}(\text{sensor reading}) + 0.38 \qquad (5.1.1)$$

The constants were chosen to emphasize accuracy in the range of the smaller openings.

Since potentiometer resistance is sensitive to temperature variations, a resistive position sensor would not be a wise choice on the final version. Alternatively, a similar sensor (perhaps capacitive) can be used without effecting the performance of the control.

5.2 Force Sensors

Force information is obtained via an array of eight strain gauges. The calculation of the contact force and contact location from the strain data was described in chapter 4. Described here is the electrical model of the strain gauges.

The strain gauges, consisting essentially of metal foil grid on a thin epoxy support, are physically coupled to the aluminum finger shaft so that any strain suffered by the finger is transmitted to the gauge. This strain gives rise to a small change in resistance which can be accurately measured. In this section a linear approximation of the relation between strain and measured output voltage is derived.

The dimensionless relationship between the change in gauge resistance and change in length is called the gauge-factor, GF, and is expressed mathematically as

$$GF = \frac{\Delta R/R}{\Delta L/L}. \tag{5.2.1}$$

Here, R and L are the nominal resistance and length respectively, and ΔR and ΔL are the changes from the nominal values which occur as the gauge is strained along the surface to which it is bonded. A large value for the gauge factor is desired since it represents a measure of strain sensitivity.

Combining equations 4.1.1 and 5.2.1 yields

$$\epsilon = \frac{\Delta R/R}{GF}. \tag{5.2.2}$$

Thus by measuring the change in resistance, the strain can be calculated.

Noted for its convenient and accurate measurements of resistance, a Wheatstone bridge (figure 5.1) is used to measure the small change in resistance of the strain gauge, R_1, which occurs as the material is strained.

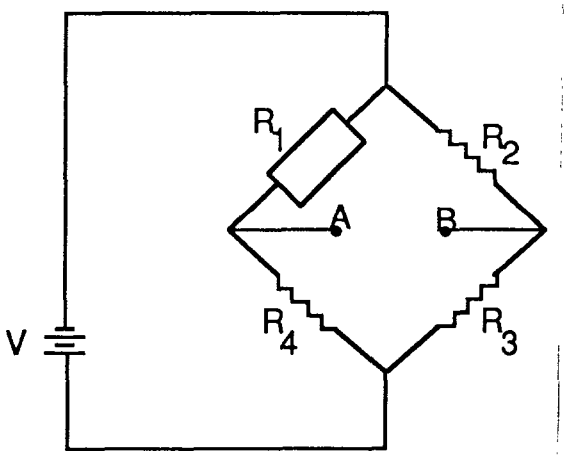

Figure 5.1: *Wheatstone Bridge*

constant	value
$R_2 = R_3 = R_4$	350 Ω
R_1 nominal	350 Ω
V	24 V
GF	2.15

Table 5.1: *Wheatstone Bridge Parameters*

Using elementary circuit theory, the voltage across the terminals A, B can be calculated as

$$V_{AB} = \frac{V(R_1R_3 - R_2R_4)}{(R_1 + R_4)(R_2 + R_3)}. \tag{5.2.3}$$

Thus it is easily seen that by proportioning the resistances as

$$\frac{R_1}{R_4} = \frac{R_2}{R_3}, \tag{5.2.4}$$

it is possible to balance the bridge such that there is no voltage difference between these terminals. Refer to table 5.1 for circuit parameters. A small change in the strain gauge resistance, R_1, from its nominal value will cause a voltage

change, ΔV_{AB} at terminals A, B which can be expressed as

$$\Delta V_{AB} = \frac{V \Delta R_1 R_3}{(R_1 + \Delta R_1 + R_4)(R_2 + R_3)} \approx \frac{V R_1 R_3}{(R_1 + R_4)(R_2 + R_3)} \frac{\Delta R_1}{R_1}. \quad (5.2.5)$$

Note that this is an approximately linear relationship for the small variations from the nominal value of the resistance R_1 which would occur as a result of strain. A conservative estimate of the maximum variation would be $|R_1| < 10\ \Omega$. Amplification is necessary since the voltage output only varies between $\pm 1.71V$ over this resistance range. The addition of the amplifier is represented mathematically by a multiplicative gain α.

Now, combining this equation with equation 5.2.2 gives the strain as a linear function of the output voltage:

$$\epsilon = \frac{(R_1 + R_4)(R_2 + R_3)}{\alpha V R_1 R_3} \frac{\Delta V_{AB}}{GF}. \quad (5.2.6)$$

Again with the aid of an A/D converter the sensor data is made available to the control algorithm. Using equation 5.2.6 together with equation 4.2.28 the holding force can be calculated for either finger. For the purpose of force control, however, the neural net approximation of the holding force will be used as discussed in chapter 4.

5.3 Neural Network

Using the experimental setup described in chapter 4, strain gauge readings

were taken for various holding forces and contact locations.[1] The tangential forces, F_x and F_y, are constrained by the experiment design to be zero. In addition, the face plate holds the z offset exactly constant. By imposing these three constraints, the problem is simplified considerably. In fact, the inverse mapping, $\widetilde{\mathbf{H}}^{-1}$, can be completely decoupled. The inverse mapping for finger 1 is as follows:

$$F_z = \frac{ba^2E(\epsilon_2 - \epsilon_1)}{6d_{12}} \tag{5.3.1}$$

$$d_y = \frac{d_{12}\epsilon_1}{(\epsilon_2 - \epsilon_1)} \tag{5.3.2}$$

$$d_x = \frac{.7ba^2G}{2E(\epsilon_2 - \epsilon_1)}(\epsilon_1(d_{12} - d_{13}) + d_{13}\epsilon_2 - 2d_{12}\epsilon_3) \tag{5.3.3}$$

The inverse mapping for finger 2 is similar.

The neural network weightings and biases for finger 1 (the long finger) were calculated by the back propagation method.[2] To account for the software requirement that all inputs and outputs of the training data set be normalized to the interval (0,1) define

$$\tilde{\epsilon}_i \triangleq (\epsilon_i + 20)/300. \tag{5.3.4}$$

The neural network mapping is then described by

$$F_z = \frac{25}{1 + \exp(-2.2 + 19.4\tilde{\epsilon}_1 - 20.8\tilde{\epsilon}_2 - .8\tilde{\epsilon}_3)} \tag{5.3.5}$$

[1] Data courtesy of Dr. Dipak Naik, Mechanical Engineering Department, University of North Carolina.

[2] The software for this was taken from the Parallel Distributed Processing Software Package by Rumelhart and McClelland.

$$d_y = \frac{8}{1+\exp(-2.2-109.8\widetilde{\epsilon_1}+85.5\widetilde{\epsilon_2}+2.3\widetilde{\epsilon_3})}+1 \qquad (5.3.6)$$

$$d_x = \frac{8}{1+\exp(1.3+11.7\widetilde{\epsilon_1}-22.6\widetilde{\epsilon_2}+31.3\widetilde{\epsilon_3})}+1. \qquad (5.3.7)$$

Plots of the actual mapping versus the the neural network mapping are given in figure 5.2. These results are comparable to those obtained by Naik and Dehoff [18] using a truncated Taylor series approximation.

The apparent error is due not only to errors in the neural net approximation of the nonlinear function, but also to the inaccuracies in the training data. Some of the inaccuracies will be eliminated by the use of higher precision components for the circuit elements such as the Wheatstone bridge and the strain gauges themselves.

5.4 Macintosh Design Environment

To facilitate rapid design and testing of control algorithms, a design environment was created using a Macintosh II (MacII) equipped with a MacAdios board for D/A and A/D conversions. Amplification of the motor control signal was necessary in order to develop enough power to drive the motor.

The time optimal position controller has been implemented. The controller can position to within $\pm.25$ cm of the desired position without overshoot. The accuracy of the positioning at various openings is reported in figure 5.4.

Several problems due to strain measurement noise have arisen while imple-

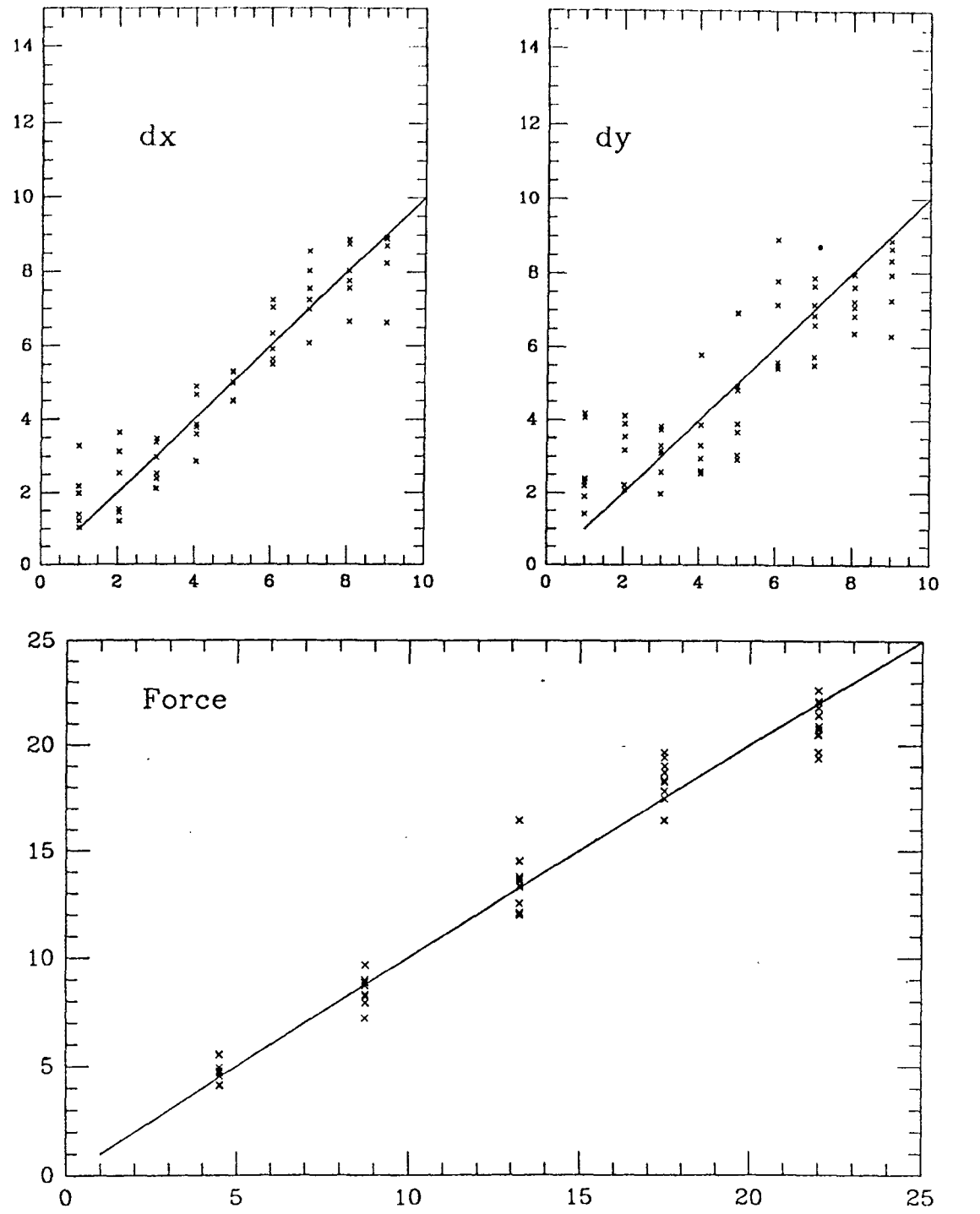

Figure 5.2: *Actual vs Calculated Values for Holding Force and Position Offset*

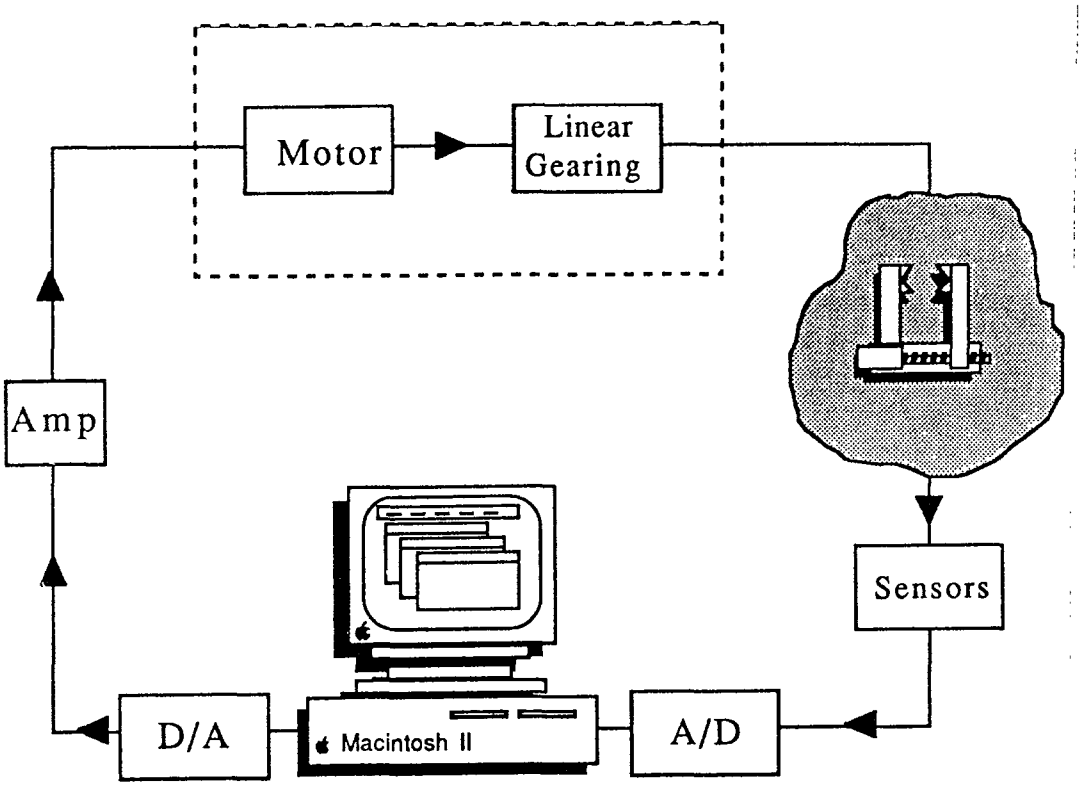

Figure 5.3: *Hardware Flow Diagram*

menting the force controller. Significant among these is strain gauge drift. Strain gauge drift is described as the tendency of the voltage output at constant strain to change value. In part, this has been contended with by adjusting amplification circuitry (tuning potentiometers) to report approximately zero voltage at zero strain. In addition, a software settable bias has been included such that the strain gauge zero may be set arbitrarily. The cause of the strain gauge drift is partially due to instability in the amplification circuitry. A significant improvement should be realized by use of higher quality components and wire wrapped circuits.

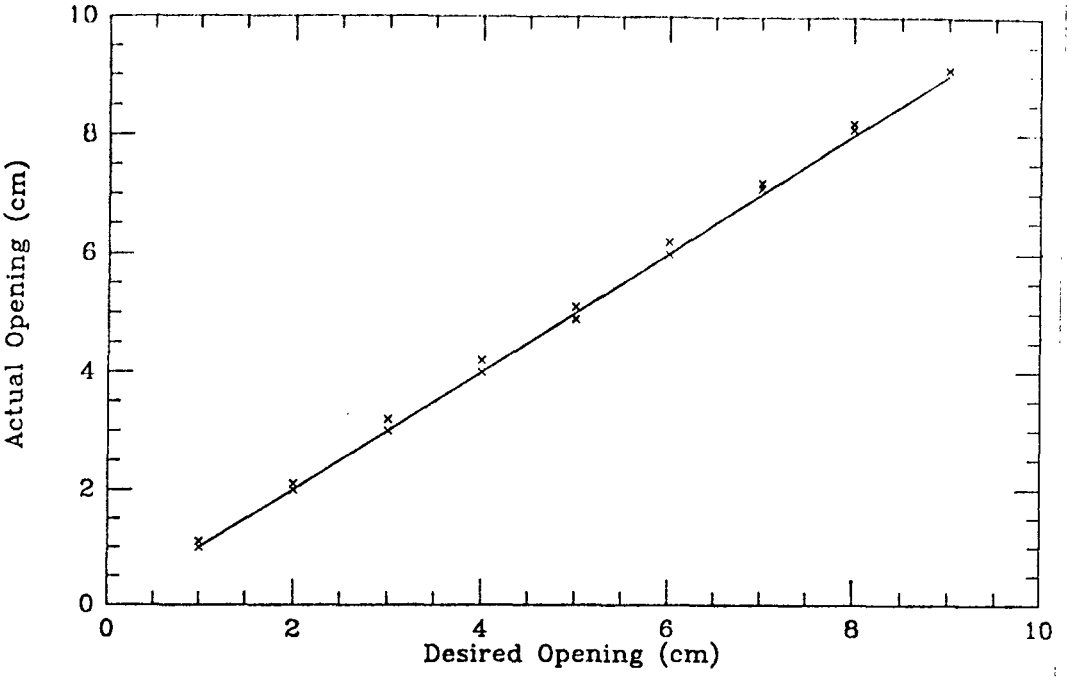

Figure 5.4: *Positioning Accuracy*

Until the noise problems have been solved, implementation of the contact force and grip point calculation algorithm is virtually impossible. Variations in the strain gauge readings will cause significant errors in the calculations since the neural network mapping is based on a certain set of training data. In spite of this the force controller has been implemented but it cannot report an accurate holding force. The operator has the option of choosing one of three levels for the holding force: high, medium, or low. Addressing the problem of hitting an unexpected obstacle, the hybrid force/position controller stops if the prespecified force level is achieved during positioning.

Although the successful implementation of the neural network approximation

constant/variable	definition
$\epsilon \in \mathbb{R}^8$	readings from eight strain gauges
$\sigma \in \mathbb{R}$	potentiometer reading
$\tilde{F}_c \in \mathbb{R}^3$	contact force estimate(x, y, and z components)
$\tilde{P}_c \in \mathbb{R}^2$	contact location estimate ((5,5) = center)
$P_d \in \mathbb{R}$	desired gripper opening
$F_d \in \mathbb{R}$	desired holding force
$\tilde{P}_d \in \mathbb{R}$	current gripper opening estimate
$\tilde{F}_d \in \mathbb{R}$	current holding force estimate
$\epsilon_a \in \mathbb{R}$	motor control voltage (armature voltage)
$M \in \mathbb{R}$	maximum armature voltage
$K \in \mathbb{R}$	force controller gain
$\tau \in \mathbb{R}$	contact force threshold, ≈ 0
$\rho \in \mathbb{R}$	contact position threshold, ≈ 0
$\delta \in \mathbb{R}$	gripper opening threshold, ≈ 0
$\eta \in \mathbb{R}$	holding force threshold, ≈ 0
$t \in \mathbb{R}$	strain threshold, ≈ 0

Table 5.2: *Controller Notation*

of the mapping from strains to contact force and contact location has not been demonstrated, the approach seems to be a good one. This method offers a simple straight forward approach to this calculation which is unchanged by additional complexity of the mapping.

The control system block diagram along with flow diagrams of the control algorithm can be found in figures 5.5-5.9. Some of the notation used in these figures is summarize in table 5.2. The estimates are calculated as described in the previous sections.

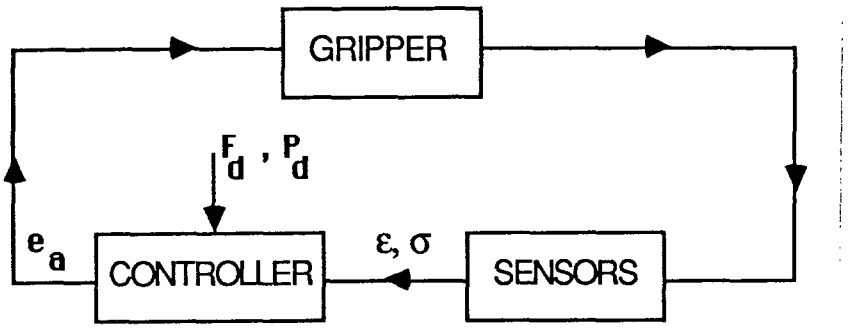

Figure 5.5: *Control System Block Diagram*

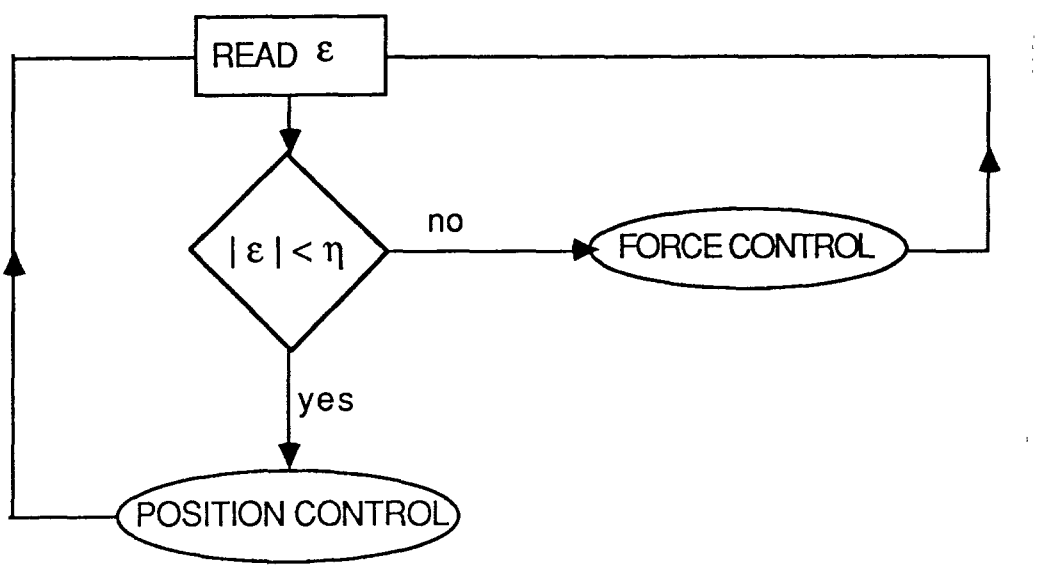

Figure 5.6: *Control Algorithm: main loop*

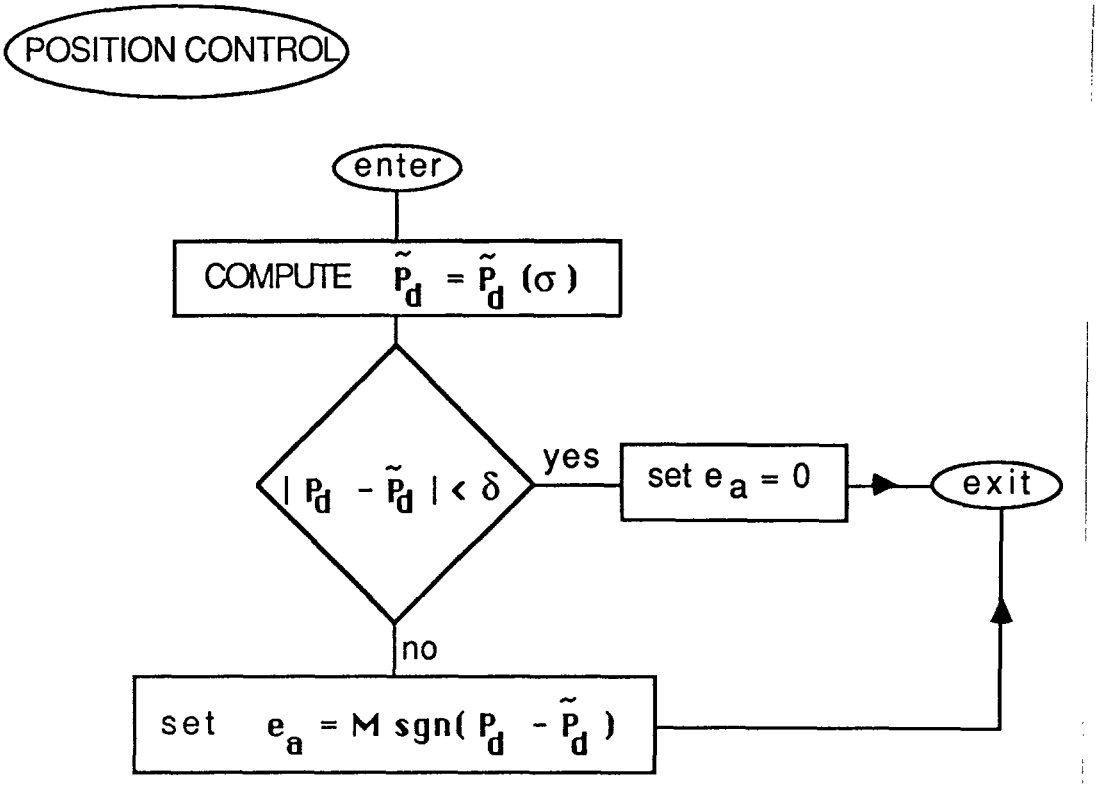

Figure 5.7: *Position Control Diagram*

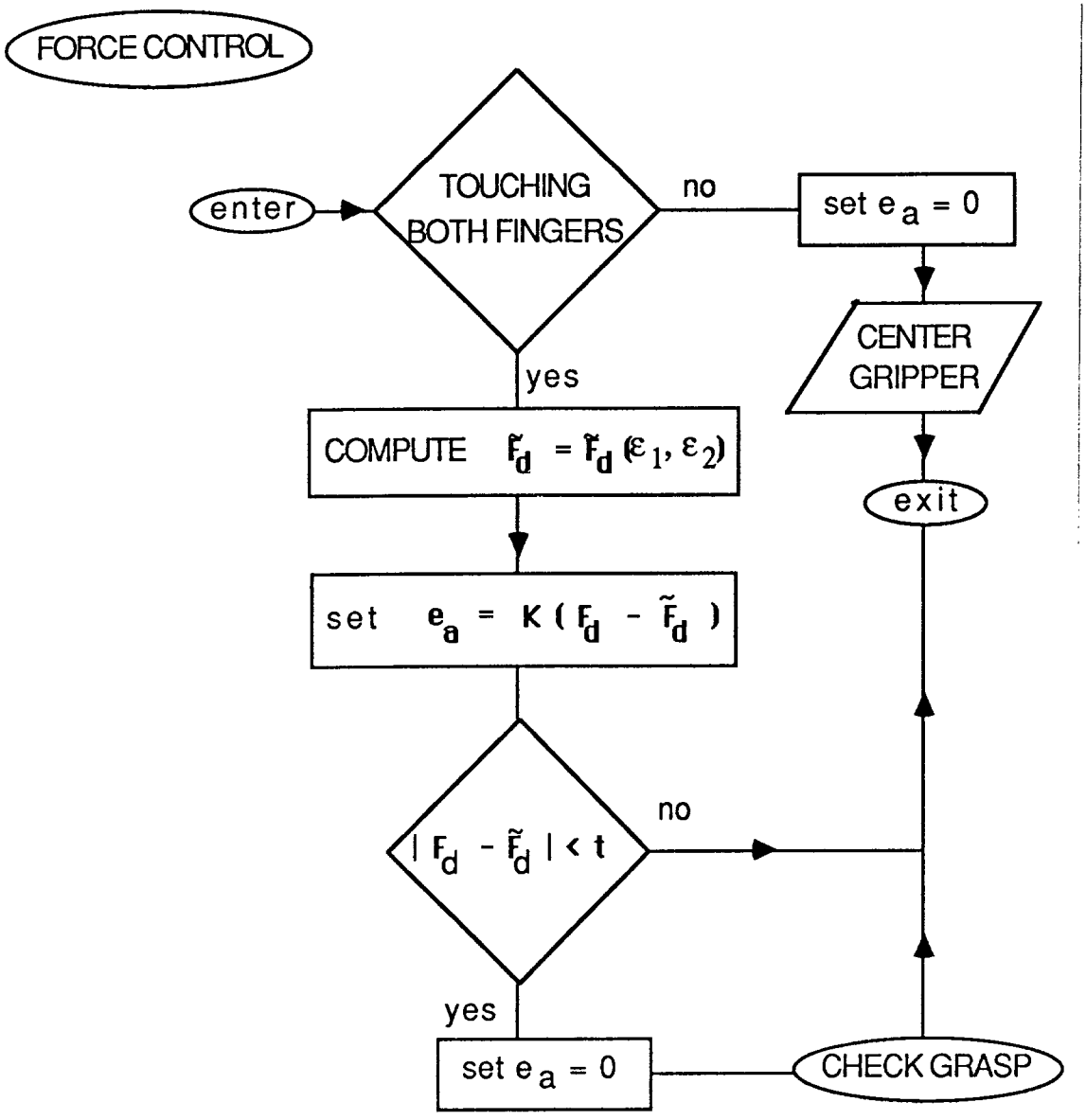

Figure 5.8: *Force Control Diagram*

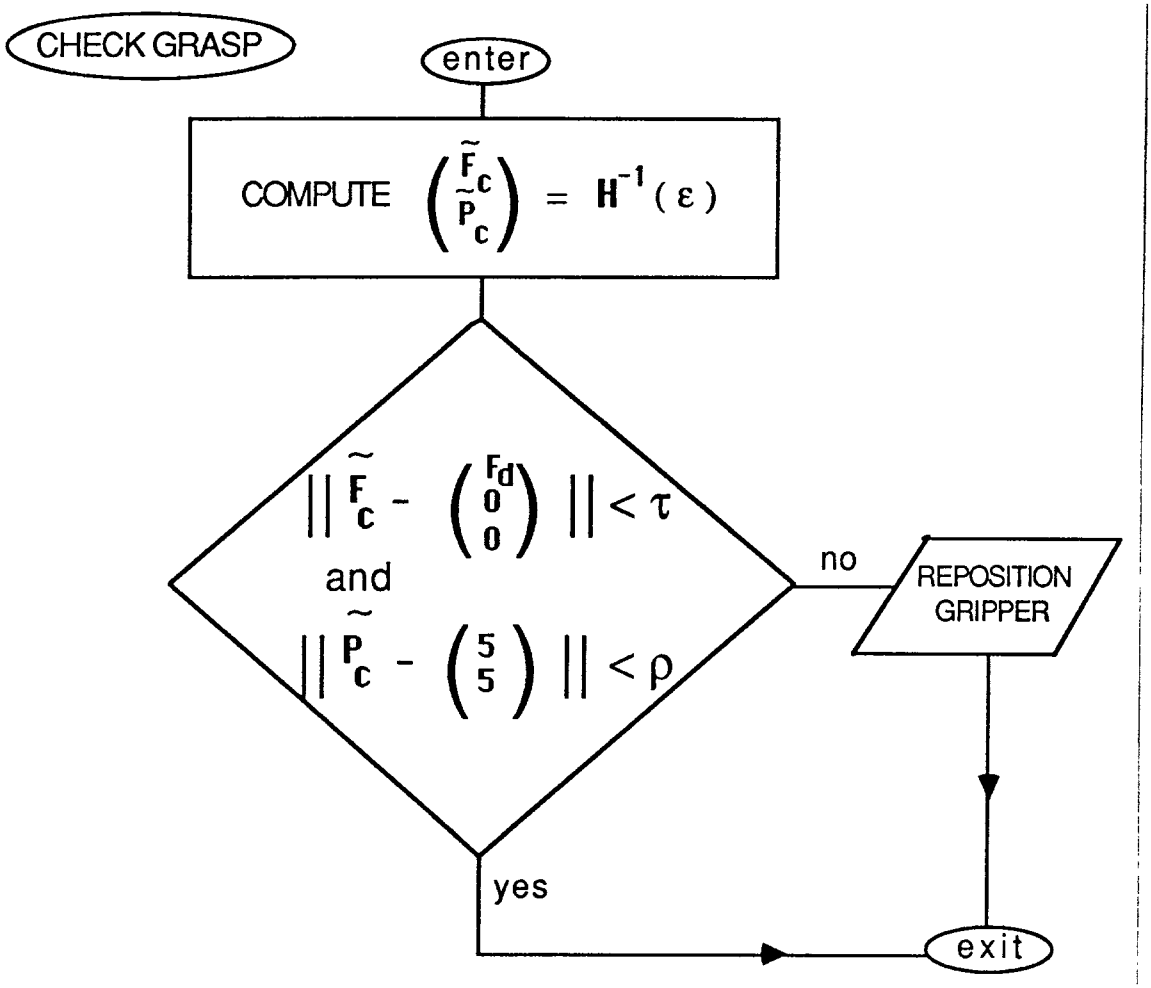

Figure 5.9: *Improper Grasp Detection*

CHAPTER

SIX

Conclusions and Future Research

A controller has been developed and tested for the gripper portion of the zero gravity robotic end effector. It was determined that an optimal control exists which transfers the initial finger opening to the desired opening in minimum time. This time optimal control is unique and is constant with value equal to plus or minus maximum armature voltage, the value of the control depending on the relative location of the desired final position.

A force controller has been developed which is based only on the holding force, perpendicular to the finger face. The holding force on either finger can be calculated from the output of two strain gauges on that finger by

$$F_z = \frac{ba^2E(\epsilon_2 - \epsilon_1)}{6d_{12}} = \frac{ba^2E(\epsilon_6 - \epsilon_5)}{6d_{12}}. \tag{6.0.1}$$

for finger 1 and 2 respectively (see figures 4.1 and 4.5). By including the output of two additional strain gauges on each finger the two tangential force components and the contact location may be calculated as well.

For the simplified case considered in chapter 5, where the tangential force components are constrained to be zero, the percent error between the actual

mapping and the neural net mapping is similar to that achieved by the truncated Taylor series used by Naik and Dehoff [18]. It would be interesting to compare the results for a more general case.

The MacII design environment has been used for controller development and testing. The next logical step is to transfer the algorithm to a dedicated signal processing chip that can communicate with the central robot controller. Exact knowledge of the communication protocol of the system is required for the completion of this; however, transfer of the control algorithms should be straight forward since they are already coded in the C programming language.

6.1 Rolling Finger Design

When positioning a multilink robotic manipulator there are unavoidable errors at each joint. Accumulation of these errors causes the largest error margins to occur at the end effector. Designed to ensure a positive locking grasp (one which does not rely on friction), the sculptured face of the gripper fingers makes them relatively intolerant to position errors. A design which incorporates a positive locking grasp with greater robustness to position error is needed.

NASA has already constructed the prototype of an improved design. These so called *rolling fingers* also boast a positive locking grasp. Allowing a position error of approximately ± 1 cm in one direction and ± 2 cm in the other, these

fingers constitute a significant improvement over the current fingers. Combined with the compliance inherent in the manipulator arm, introduction of roller bearings on the face of the fingers improves the manipulator robustness with respect to position error.

Although these new fingers demand analysis in their own right, the application of the work presented in this thesis is direct.

Appendix

A

Feed Forward Neural Networks

A neural network can be completely specified by three basic components: the neuron characteristics, the topology and the training or learning rule.

The simplest computational element, or neuron, forms a weighted sum of inputs and passes the result through a nonlinearity. The inputs may be network inputs, or outputs of other neurons, depending on the topology. The neuron is characterized by an internal threshold or offset θ and by the type of nonlinearity. The nonlinearity used in this application is the sigmoid logistic nonlinearity:

$$f(\alpha) = \frac{1}{1 + \exp(\theta - \alpha)}. \tag{1.0.1}$$

The topology describes the manner in which the neurons are interconnected. A basic problem with using a neural network to perform a particular task is that little is know about the required complexity of the network topology, or which topology is best suited for the task. It has been shown by Cybenko [11], that continuous functions of finite support may be approximated by a feed forward neural network with a single (finite) hidden layer. It is thus justified that this

topology be used here. A feed-forward network is arranged in layers such that the outputs of one layer serve as the inputs to the next layer. Neurons within a layer are not connected in any way.

An example of supervised learning, the backpropagation algorithm is a means for using the training data set to adjust the network weights and biases in a multilayer feed-forward neural network. The algorithm is actually an implementation of recursive gradient descent procedure to minimize the mean square error between the networks actual output and the desired output. If the network has hidden units, then the error function is no longer convex and there is a danger of getting stuck at a local minima. However, this algorithm has been used successfully in a wide variety of tasks.

A recursive algorithm to adjust the weights, starting at the output nodes and working back to the first hidden layer, is given in reference [13] for the case of the sigmoid logistic function. A generalization for arbitrary networks can be found in reference [10].

BIBLIOGRAPHY

[1] K. Ogata, *Modern Control Engineering.* Elglewood Cliffs, NJ: Prentice Hall, 1970.

[2] Electrocraft Corporation, ed., *DC Motors, Speed Controls, Servo Systems.* Elmsfor, NY: Pergamon Press, fifth ed., 1980.

[3] M. Athans and P. Falb, *OPTIMAL CONTROLS: An Introduction to the Theory and It's Applications.* New York, NY: McGraw-Hill, 1966.

[4] M. Fan, L. Wang, J. Koninckx, and A. Tits, "CONSOLE Users Manual," Tech. Rep. 87-212, Systems Research Center, 1987.

[5] K. Astrom, "A SIMNON tutorial," Tech. Rep., Lund Institute Of Technology, July 1985.

[6] A. Window and G. Holister, eds., *Strain Gauge Technology.* Essex, England: Applied Science Publishers, 1982.

[7] T. Beckwith, N. Back, and R. Marangoni, *Mechanical Measurements.* Reading, MA: Addison-Wesley, third ed., 1982.

[8] S. Timoshenko and J. Gere, *Mechanics of Materials.* New York, NY: Van Nostrand Reinhold Company, 1972.

[9] M. Spotts, *Design of Machine Elements.* Englewood Cliffs, NJ: Prentice-Hall, Inc., sixth ed., 1985.

[10] D. Rumelhart and G. McClelland, *Parallel Distributed Processing: Explorations in the Microstructure of Cognition.* Cambridge, Ma.: MIT Press, 1988.

[11] G. Cybenko, "Approximation by superpositions of a sigmoidal function," Technical Report, Tufts University, Department of Computer Science, October 1988.

[12] B. Anderson and J. Moore, *Linear Optimal Control.* Elglewood Cliffs, NJ: Prentice Hall, 1975.

[13] R. P. Lippmann, "An introduction to computing with neural nets," *IEEE ASSP Magazine.*, pp. 4–22, April 1987.

[14] C. Chen, *Linear Systems Theory and Design.* New York, NY: Holt, Reinhard and Winston, 1984.

[15] S. Timoshenko and D. Young, *Elements of Strength of Materials.* Princeton, NJ: D. Van Nostrand Company, Inc., 1968.

[16] C. Close and D. Frederic, *Modeling and Analysis of Dynamic Systems.* Boston, MA: Houghton Mifflin Company, 1978.

[17] J. Nilsson, *Electric Circuits.* Reading, MA: Addison-Wesley, 1983.

[18] D. Niak and P. Dehoff, "Design of an Auto Change Mechanism and Intelligent Gripper for the Space Station," Tech. Rep. NAG 5-922, NASA Goddard, 1989.

[19] C. Perry and H. Lissner, *The Strain Gage Primer.* New York, NY: McGraw-Hill, 1955.

[20] Measurements Group, Inc, *Errors Due to Misalignment of Strain Gages.* 1983.

[21] Measurements Group, Inc, *Plane Shear Measurements with Strain Gages.* 1983.

[22] Measurements Group, Inc, *Errors Due to Transverse Sensitivity Strain Gages.* 1982.

[23] Measurements Group, Inc, *Noise Control in Strain Gage Measurements.* 1980.

[24] Measurements Group, Inc, *Optimizing Strain Gage Excitation Levels.* 1979.